Scientific Reports

https://doi.org/10.1038/s41598-026-35050-2

Article in Press

Disruption of NLRP3 inflammasome assembly via ligand-induced remodeling of pyrin domain interfaces

Received: 19 August 2025

Accepted: 1 January 2026

Published online: 09 January 2026

Cite this article as: Khosravifard S., Hosseinkhani S., Bakhtiary N. *et al.* Disruption of NLRP3 inflammasome assembly via ligand-induced remodeling of pyrin domain interfaces. *Sci Rep* (2026). https://doi.org/10.1038/s41598-026-35050-2

Sara Khosravifard, Saman Hosseinkhani, Nuredin Bakhtiary, Maryam Peyvandi & Alexander S. S. Dömling

Disruption of NLRP3 Inflammasome Assembly via Ligand-Induced Remodeling of Pyrin Domain Interfaces

Sara Khosravifard[1], Saman Hosseinkhani[2*], Nuredin Bakhtiary[1], Maryam Peyvandi[1], Alexander S.S. Dömling[3,4]

[1]Department of Biochemistry, Faculty of Biological Sciences, NT.C, Islamic Azad University, Tehran, Iran

[2]Department of Biochemistry, Faculty of Biological Sciences, Tarbiat Modares University, Tehran, Iran ö

[3]Institute of Molecular and Translational Medicine/Department of Medical Biophysics, Faculty of Medicine and Dentistry, Palacký University and University Hospital Olomouc, Hněvotínská 1333/5, 779 00 Olomouc, Czech Republic

[4]Czech Advanced Technologies and Research Institute (CATRIN), and Institute of Molecular and Translational Medicine (IMTM), Palacký University Olomouc, Křížkovského 511/8, 779 00, Olomouc, Czech Republic

***Corresponding author:** Saman Hosseinkhani, Email: Saman_h@modares.ac.ir

Abstract

The inflammasome is a multimeric intracellular complex that regulates caspase-1 activity in innate immunity, with NLRP3 serving as a central mediator of inflammatory responses. Despite extensive efforts, effective inhibitors of NLRP3 oligomerization remain limited. Here, we screened a library of small molecules and identified four candidates that disrupt homo-oligomerization of the NLRP3 pyrin domain (PYD). Among these, compound E9 exhibited superior affinity and specificity, as confirmed by split-luciferase complementation assays, microscale thermophoresis (Kd < 1 μM), molecular docking, and molecular dynamics simulations. Mechanistic analyses revealed that E9 binding induces targeted structural and dynamic remodeling of the PYD filament, dampening dominant collective motions and disrupting cooperative inter-subunit interactions. These changes reduce the filament's conformational flexibility and impair its ability to recruit ASC, thereby inhibiting inflammasome activation in THP1-ASC-GFP cells, as evidenced by suppression of speck formation. Overall, our study identifies E9 as a potent inhibitor of NLRP3 oligomerization and highlights interface-specific modulation of filament dynamics as a promising strategy for developing next-generation inflammasome-targeted therapeutics.

Keywords: Pyroptosis; NLRP3 inflammasome; Pyrin domains; Split luciferase assay; Microscale thermophoresis

Introduction

Among the inflammasomes characterized in innate immunity, NLRP3 is the most extensively studied, owing to its capacity to sense a diverse array of pathogen-associated and damage-associated molecular patterns (PAMPs and DAMPs) [1–4]. The NLRP3 inflammasome is a key component of the innate immune system, activated by a wide range of stimuli, including pathogen-associated molecular patterns (PAMPs) and danger-associated molecular patterns (DAMPs) [1, 5]. Upon activation, caspase-1 is recruited and initiates the maturation of pro-inflammatory cytokines such as interleukin-1β (IL-1β) and interleukin-18 (IL-18), both of which play critical roles in orchestrating innate immune responses [6]. Owing to its central role in numerous inflammatory diseases [6, 7], the NLRP3 inflammasome has garnered significant attention as a potential therapeutic target. The NLRP3 inflammasome, a cytosolic protein assembly that a key component of the innate immune system, plays a critical role in detecting and responding to a wide range of stimuli upon activation by microbial invasion, environmental insults or oxidative stress, trigger a cascade of inflammatory events critical for pathogen elimination and maintenance of tissue homeostasis [8, 9]. It consists of three primary components: the NLRP3 sensor protein, the adaptor ASC (apoptosis-associated speck-like protein containing a caspase recruitment domain), and pro-caspase-1 [6, 10-15]. Each of these elements contributes distinctively to the assembly and activation of the inflammasome complex.

Structurally, NLRP3 contains three key domains: an N-terminal pyrin domain (PYD), a central NACHT domain required for oligomerization [16], and a C-terminal leucine-rich repeat (LRR) domain. Upon activation, NLRP3 undergoes homo-oligomerization [16, 17], forming a disk-like structure via PYD–PYD interactions. This multimeric scaffold then recruits ASC through PYD–PYD engagement [18, 19], which in turn recruits pro-caspase-1 via CARD–CARD interactions

[15, 20, 21]. The resulting NLRP3–ASC–pro-caspase-1 complex is essential for the activation of caspase-1 and the initiation of downstream inflammatory responses [14, 15, 22].

As a multiprotein signaling platform, the NLRP3 inflammasome drives caspase-1 activation and the release of key cytokines, and its dysregulation underlies numerous inflammatory diseases [2, 23]. Preclinical efforts using small molecules, natural compounds, and biologic inhibitors of NLRP3, such as JC124, MCC950, and CY-09, have been developed. These efforts have successfully attenuated chronic inflammation and tissue damage [7, 24]. Such targeted strategies offer promising therapeutic avenues for conditions marked by persistent, unresolved inflammation [25, 26].

However, most current anti-inflammatory treatments primarily focus on neutralizing IL-1β or IL-18, often overlooking the broader inflammatory signaling pathways initiated by NLRP3 or its potential crosstalk with other inflammasomes [27, 28]. Despite substantial research into inhibitors targeting various components of the inflammasome complex, specific molecules that disrupt NLRP3 homo-interactions remain limited. Prior studies have characterized the self-associative properties of the NLRP3 PYD domain and its sensitivity to protein and salt concentrations [27, 29]. However, the exact role of NLRP3 PYD homo-interactions in inflammasome activation remains poorly defined. Current inhibitors such as CY-09 and MCC950 act by binding to the ATP-binding motif within the NLRP3 NACHT domain, but do not directly interfere with PYD-PYD interactions [27, 29, 30]. This highlights a knowledge gap in the existing research on this topic.

A deeper understanding of NLRP3's structural components and activation mechanisms is therefore essential for the advancement of targeted therapies. In this context, our study explores an innovative strategy by identifying novel compounds that specifically interfere with NLRP3 PYD (pyrin domain) interactions—offering a distinct therapeutic approach from traditional cytokine-

based interventions. Leveraging advanced screening technologies, we aim to discover new pharmacological agents with the potential to transform treatment paradigms for inflammasome-mediated inflammatory disorders [5, 8, 31].

The split-luciferase complementation assay has proven versatile in detecting protein–protein interactions across several cell death pathways, including apoptosis, necroptosis, and pyroptosis [32, 33]. This approach has also been applied to monitor NLRP3 PYD interactions as a proxy for pyroptotic activation. Using this technique, researchers have successfully identified novel inhibitors—QM380 and QM381—through screening of chemical libraries [32, 34–37].

Inflammasome formation takes place through assembly of Pyd domain of NLRP3 and based on 7PZD Cryo-EM structure, they form a filament-like gathering with symmetric interactions between all six surfaces (Ia–Ib, IIa–IIb, IIIa–IIIb), as indicated in Fig. 1.

In this study, we aimed to identify small molecules that disrupt NLRP3 PYD–PYD interactions. We screened a library of 1,500 newly synthesized small molecules using a reconstituted split-luciferase assay. This system employs luciferase fragments fused to interacting proteins, generating a robust, low-background luminescent signal upon interaction [32, 38–40]. Based on luciferase signal reduction, four hit compounds were selected for further validation using microscale thermophoresis (MST) and molecular docking analyses [41, 42]. Notably, one compound (E9) exhibited significant inflammasome-inhibitory activity in cell-based inflammation models, as investigated by cell-based assay and molecular dynamic simulations.

Results

Expression and purification of reporter proteins

After initial expression and purification of Nluc-PYD and Clu-PYD (Fig. 2, Fig. S1), we observed that the interaction between NLRP3 PYD domains led to the reconstitution of firefly luciferase activity, resulting in luminescence, irrespective of the presence of certain compounds (data not shown). Luciferase activity was measured by mixing the purified protein constructs. Individual luciferase fragments alone did not generate detectable luminescence. Moreover, the NLRP3 PYD S5D mutant, which is incapable of forming homotypic interactions, exhibited no luminescence, indicating that luciferase activity restoration depended on proper alignment and constitutive interaction of the PYD domains. In contrast, combining both luciferase fragments produced a strong luminescent signal, consistent with NLRP3 PYD oligomerization observed in previous studies.

Screening of a library of chemical compounds

Among 1,500 compounds screened, four—located at positions E2, E9, B1, and G3 on plate No. 13—elicited a marked decrease in luminescence in our NLRP3 PYD interaction assay versus the no-compound control (Fig. 3). Notably, even in the absence of inhibitors, reconstituted luciferase activity rose steadily over the first 12 minutes, reflecting the assay's intrinsic kinetics. B1 and G3 showed only transient inhibition: an initial drop in luminescence was followed by a rebound, whereas E9 maintained robust suppression at every time point (Fig. 3). Dose–response analyses (Fig. 4) revealed a classic sigmoidal inhibition curve for E9, and among the four hits, only E2 and E9 (Fig. 5) produced significant, concentration-dependent decreases in luminescence (Fig. 4 and structures shown in Fig. 5). Importantly, none of these compounds affected native luciferase activity (data not shown), underscoring their specificity for disrupting PYD–PYD interactions.

Microscale Thermophoresis (MST) analysis

Microscale thermophoresis was employed to quantify binding between the NLRP3 pyrin-domain dimer (PYD–PYD) and our selected small molecules. To validate the assay, we first compared the thermophoretic behavior of the wild-type and S5D-mutant PYD constructs. Interaction of both native and mutants NLuc-NLRP3PYD to CLuc-NLRP3PYD proteins yielded sigmoidal binding curves, respectively. However, as indicated in Fig. 6, the disruptive S5D mutant exhibited both a shifted curve and a significantly altered dissociation constant (Kd) relative to the native dimer (Fig. 6), confirming that MST sensitively reports on PYD conformational integrity.

Having established assay performance, we next focused on ligand screening using CLuc-PYD as the fixed target. Protein and ligand concentrations were held at 50 nM and 200 μM, respectively, across all titrations. Of the four candidates tested, E2 and E9 produced markedly lower Kd values, correlating with pronounced decreases in CLuc luminescence (Fig. 7). Follow-up dose–response measurements at 25 °C and 45 °C reinforced their strong inhibitory profiles: both compounds bound PYD with submicromolar affinities (Kd < 1 μM; Table 1). MST traces and capillary scans of selected compounds with their shown dose-response curves are indicated in Fig. S5.

These results not only validate MST as a robust platform for interrogating PYD–ligand interactions but also highlight E2 and E9 as potent inhibitors of NLRP3 PYD dimerization.

Table 1. The average Kd (μM) for four selected ligands at two different temperatures.

	25 (ºC)	**45 (ºC)**
B1	8.2	Not obtained
G3	43	3.9
E2	0.7	0.1
E9	0.01	0.08

ASC Speck Formation as an Indicator of Inflammasome Assembly

To assess the impact of candidate compounds on PYD–PYD interactions, we initially confirmed the effectiveness of compound E9 in inhibiting NLRP3-PYD homo-oligomerization in a cell-free in vitro system. We then evaluated whether E9 could suppress pyroptosis and inflammatory signaling by monitoring ASC speck formation, a hallmark of inflammasome assembly as a live cell-based assay (Fig. 8).

Using THP1-ASC-GFP cells—a THP-1-derived monocytic cell line stably expressing ASC-GFP under the NF-κB promoter—we examined the effects of E2, E9, and previously identified inhibitors (QM381 and MCC950) on ASC speck formation. As indicated in Fig. 8, E9 in a specific time point could be able to reduce the number of formed speck, similar to the action of QM381 and MCC950. Upon lipopolysaccharide (LPS) stimulation, ASC-GFP is expressed and evenly distributed in the cytoplasm. Subsequent treatment with nigericin activates the NLRP3 inflammasome, leading to visible ASC-GFP speck formation. The extent of speck formation was quantified using fluorescence microscopy. More details of experimental results are shown in Fig. S2 and Fig. S3.

Molecular Docking

To investigate the structural basis of ligand interactions with the pyrin domain (PYD) of NLRP3, we performed molecular docking using AutoDock Vina, followed by experimental validation. Interaction patterns of the four selected compounds were analyzed using LigPlot and are summarized in Fig. **5**. The calculated binding energies were -8.5, -8.0, -7.6, and -5.5 kcal/mol for compounds E2, B1, E9, and G3, respectively. Among these, E2 and B1 exhibited the most favorable binding energies, whereas E9 formed the highest number of interactions with key interface regions: IIb (green), IIa (magenta), and IIIa (yellow).

A comparative analysis of the chemical structures and binding energies of the ligands, alongside the docking results and their specific interaction profiles with the PYD domain, is detailed in Table 2. Critical interface residues mediating NLRP3 PYD homo-dimerization include residues from the Ia interface (Ser5, Arg7, Cys8, Glu15, Asp60, Val52, and His51) and Ib interface (Lys36, Arg43, Met27, His28, Glu30, and Asp31). Additional interactions involve Asp60 (IIa) and Asp82 (IIb), and Phe61 (IIa) with Arg81 (IIb). Furthermore, Arg43 from IIIa interface forms two salt bridges with Glu18 from IIIb, while Pro42 and Gln45 (IIIa) interact with Asp16 and Glu15 (IIIb), respectively.

Docking analyses of pyrin domains in the presence of selected ligands were conducted to assess binding interactions. Structural investigations revealed that the first compound (B1) does not bind within the primary junction regions of the pyrin domains. Similarly, the second compound (G3) exhibits a binding pattern identical to B1, with its residues located outside the main interfacial zones.

Structural and Dynamic Impact of E9 Binding on NLRP3PYD Filament

To investigate the structural and dynamic consequences of E9 ligand binding to the NLRP3PYD filament subunit, molecular dynamics simulations were performed on both native and ligand-bound states (Fig. 9), followed by comprehensive multi-parametric analyses. Global stability metrics revealed that the ligand-bound state exhibited elevated backbone fluctuations and a modest increase in radius of gyration (Fig. 10A–B), indicating a more flexible and less compact architecture. These changes were further supported by the residue-level RMSF analysis (Fig. 10C),

which pinpointed enhanced fluctuations at the interfacial regions, particularly within Monomer II, suggesting localized destabilization upon ligand engagement. Ligand RMSD analysis showing ligand movement and internal conformational changes over the MD trajectory and disruption of NLRP3 inflammasome assembly during time (Fig. 11 A-D).

To assess the impact of ligand binding on filament dynamics, principal component analysis (Fig.12) was conducted. The results showed attenuated PC1 fluctuations and restricted conformational sampling in the ligand-bound state, as evidenced by the tighter clustering in the PCA scatter plots. This shift in dynamic behavior implies that E9 binding dampens the dominant collective motions and imposes structural constraints across the filament. Dynamic cross-correlation matrices (DCCMs), whose values range from –1 (perfectly anti-correlated) to +1 (perfectly correlated), revealed pronounced ligand-induced rearrangements in both intra- and inter-monomer dynamical relationships across the trimer (Fig. 13). In the Apo state, Monomers I, II, and III displayed mixed patterns of positive and negative correlations within their respective intra-monomer blocks (I/I, II/II, III/III), and moderate coupling across the I/II, I/III, and II/III interface blocks (Fig. 13A). Upon ligand binding, substantial changes emerged in the ligand-contacting monomers (II and III). The II/II and III/III intra-monomer blocks exhibited qualitatively altered correlation distributions, indicating a reorganization of internal fluctuation patterns.

In addition, the II–III inter-monomer block showed a marked expansion of strongly positive correlations (bright-yellow regions), reflecting increased coordinated motion between these two monomers. Monomer I responded differently, its intra-monomer block (I/I) displayed expanded regions of positive correlation, indicating heightened internal coherence of residue fluctuations. In contrast, both the I/II and I/III inter-monomer blocks exhibited broadened anti-correlated regions (blue areas), representing an increase in out-of-phase motion between Monomer I and the ligand-bound monomers II and III. Three-dimensional structural correlation networks corroborated these observations: in the Ligand-Bound state, strongly correlated residue pairs (represented by red connecting lines) were concentrated at the II–III interface, spatially aligned with the ligand-binding region, whereas interfaces involving Monomer I displayed reduced correlated connectivity. Collectively, the data show that ligand binding reorganizes both intra- and inter-monomer correlation patterns, strengthens local coupling between Monomers II and III, and alters the interfacial communication pathways associated with Monomer I. Structural correlation mapping reinforces these matrix-level observations (Fig. 13 B). In the 3D networks, red lines represent strongly correlated residue pairs and provide a spatially intuitive view of how dynamical couplings redistribute in response to ligand binding. In Monomer I, dense accumulation of red lines appears consistent with a dynamic isolation and effective decoupling of Monomer I from the filament

core. Conversely, the reduction of extensive internal red-line networks within Monomer III coincides with their redistribution across the II, consistent with strengthened inter-monomer coupling. The ligand—shown as a green mesh— acts as a dynamic bridge that locally stabilizes the II–III core.

Secondary structure evolution analysis (Fig. 14) provides further insight into local structural rearrangements. In the ligand-bound state, residues 30–55 of Monomer II underwent frequent transitions from helices to coils and coils to sheets, in contrast to the native filament, which maintained a stable helical content. These observations suggest that E9 binding induces localized unfolding and increases the structural plasticity in critical interfacial regions.

Structural overlays and ligand RMSD tracking (Fig. 15A–C) confirmed the significant conformational displacement of Monomer II after ligand binding. LigPlot analysis (Fig. 15D) identified key hydrophobic interactions anchoring E9 at the filament interface, highlighting the specific contact residues involved in stabilizing the ligand. This was further corroborated by the per-residue contact mapping (Fig. S4), which revealed persistent and spatially distinct ligand interactions in Monomers II and III, with negligible engagement in Monomer I, underscoring the asymmetric nature of ligand recognition within the filament.

Finally, atomic-level interaction profiling (Table 2) revealed multiple non-bonded contacts between E9 and filament residues. Blue-highlighted entries correspond to interface Ib, green-highlighted entries mark interface IIb, and orange-highlighted entries indicate residues from interface IIIa—collectively reflecting distinct ligand-binding zones. The observed contact pattern diverges from that of the native filament, suggesting ligand-induced reorganization of interfacial surfaces and localized structural remodeling.

Table 2. Non-bonded contacts between the NLRP3-PYD subunit and the E9 ligand in the post-MD simulation structure. The table lists atom-level interactions between the filament subunit and the E9 ligand, including residue identity and interatomic distances. Green highlights indicate residues from interface Ib, cyan highlights mark residues from interface IIb, and yellow highlights represent residues from interface IIIa—corresponding to the interface colors used in the updated figure.

	NlRP3PYD subunit					E9 ligand		
Number	**Atom number**	**Atom name**	**Residue name**	**Residue number**	**Chain**	**Atom number**	**Atom name**	**Distance**
1	1313	NE	ARG	81	II	4711	C10	3.87
2	1315	CZ	ARG	81	II	4711	C10	3.69
3	1316	NH1	ARG	81	II	4711	C10	3.76
4	1328	CB	ASP	82	II	4692	O	3.50
5	1328	CB	ASP	82	II	4725	C14	3.80
6	1460	CZ	ARG	89	II	4740	C22	3.70
7	1461	NH1	ARG	89	II	4738	C21	3.42
8	1461	NH1	ARG	89	II	4740	C22	3.31
9	1464	NH2	ARG	89	II	4740	C22	3.55
10	1464	NH2	ARG	89	II	4742	C23	3.34
11	1464	NH2	ARG	89	II	4744	C24	3.71
12	3633	O	GLU	30	III	4721	C13	3.08
13	3648	O	ASP	31	III	4721	C13	3.72
14	3660	O	TYR	32	III	4721	C13	3.37
15	3695	CB	PRO	34	III	4748	O2	3.77
16	3698	CG	PRO	34	III	4729	C16	3.76
17	3698	CG	PRO	34	III	4730	C17	3.55
18	3698	CG	PRO	34	III	4731	C18	3.71
19	3698	CG	PRO	34	III	4748	O2	3.82
20	3701	CD	PRO	34	III	4717	C11	3.74
21	3701	CD	PRO	34	III	4718	O1	3.57
22	3701	CD	PRO	34	III	4731	C18	3.81
23	3772	CG2	ILE	39	III	4734	C19	3.86
24	3791	CD	PRO	40	III	4727	C15	3.78

Discussion

The NLRP3 inflammasome plays a critical role in various pathological processes and is implicated in a broad spectrum of diseases [2]. The study emphasizes previous findings in the necessity of proper molecular orientation and constructive interactions in triggering split-luciferase activity. Utilizing complementary split-luciferase assays offers valuable insights into NLRP3 interaction dynamics and serves as a robust platform for screening of potential therapeutic inhibitors [32]. Among the 1,500 compounds tested, the E9 ligand demonstrated the most pronounced inhibitory effect, reflected by a significant reduction in luminescence-suggesting a strong interaction with the PYD domain of NLRP3 (Fig. 4). Our comparative analysis demonstrates that E9 exhibits superior affinity and inhibitory activity relative to other tested ligands, particularly at elevated temperatures (Fig. 7; Table 1). While MST results confirmed that NLRP3 PYD mutants interact differently from their native counterparts (Fig. 6), this study primarily relies on computational predictions and luminescence assays involving the native NLRP3 PYD domain.

Dose-response assays using microscale thermophoresis (MST) revealed a dissociation constant (Kd) of less than 1.0 μM for E9, indicating high binding affinity (Table 1). Notably, the lower Kd values of E9 and E2 ligands suggest a stronger binding affinity to the pyrin domain compared to B1 and G3 (Fig. 7, Table 1).

We demonstrated that E9, similar to the QM381 compound, directly interferes with NLRP3-PYD homo-oligomerization, thereby reducing ASC oligomer formation and subsequent activation of inflammatory signaling, as evidenced by the decreased number of speck formations (Fig. 8). These findings support the role of the NLRP3-PYD domain as a critical homo-oligomerization platform for ASC speck assembly. Notably, E9 appears to be a more potent inhibitor in biochemical assays compared to E2. However, it may be suggested that decrease of the number of formed speck after

a while could be due to the induction of pyroptotic cell death as indicated in other studies (Fig. 8B).

These methods, while informative, may not fully capture the complexity of protein interactions under physiological conditions. The findings for E9 align with previous reports on small-molecule NLRP3 inhibitors [18, 27]; however, further validation through comprehensive biochemical assays and clinical investigations is essential to substantiate these results. Moreover, structural optimization aimed at enhancing ligand affinity and selectivity could lead to more potent inhibitors.

Investigating additional residues within the PYD domain may also uncover novel targets for therapeutic development. This study identified potent interacting compound with interface residues between two monomers as potential ligands for targeting inflammasome.

Experimental results were further investigated by bioinformatics tools. The docking results corroborate our experimental findings, demonstrating that the E9 ligand modulates the NLRP3-PYD interaction via electrostatic forces, ultimately disrupting NLRP3-PYD monomer associations. Combined structural and docking analyses, alongside microscale thermophoresis (MST), suggest that E9 either directly binds to or interferes with NLRP3-PYD homooligomerization, thereby attenuating inflammasome complex formation.

Molecular dynamics simulations offer a powerful framework for evaluating the structural and dynamic consequences of small-molecule engagement with supramolecular assemblies. In the case of the NLRP3PYD filament—which relies on a network of symmetric interfacial interactions across six surfaces (Ia–Ib, IIa–IIb, IIIa–IIIb) to maintain its oligomeric architecture—even subtle perturbations at these interfaces can propagate destabilizing effects throughout the assembly. Ligand engagement at these sites, as modeled with compound E9, reveals a shift in the assembly's

dynamic equilibrium, highlighting the sensitivity of the PYD scaffold to targeted interfacial perturbation (Fig. 10).

The observed structural remodeling—including localized backbone fluctuations and secondary structure transitions—indicates that ligand binding can compromise the geometric precision required for ASC recruitment and inflammasome activation (Fig. 11). These effects appear to be spatially confined rather than globally disruptive, suggesting that filament destabilization proceeds through interface-specific mechanisms. This structural constraint is robustly quantified by Principal Component Analysis (PCA): The Ligand-Bound ensemble exhibits marked attenuation of fluctuations in the dominant collective motion mode (PC1) and a significantly compressed conformational space in the PC1/PC2/PC3 phase plots. This confirms that, despite localized motion, E9 binding effectively dampens the assembly's largest amplitude motions, leading to greater structural constraint (Fig. 12).

DCCM results collectively demonstrate the asymmetric mechanistic basis for this dynamic constraint and structural remodeling: Ligand binding does not uniformly rigidify the trimer but instead drives a targeted, asymmetric reorganization of its dynamical architecture. Monomers II and III form a ligand-stabilized cooperative core characterized by enhanced positive coupling and rewired intra-monomer communication pathways. This stabilization, however, produces compensatory mechanical and dynamical consequences for Monomer I: as the II–III core becomes more cohesive, Monomer I is biased into anti-phase motions relative to the core and progressively loses synchronized communication with the filament (Fig. 13).

This asymmetric dynamic partitioning is central to the disruptive mechanism and directly explains the PCA findings. The accumulation of correlated residue pairs at Monomer I's interfaces and the emergence of extensive anti-correlation patterns in the DCCM reflect a stress-driven dynamic

decoupling, consistent with an allosteric mechanism in which ligand binding reshapes long-range communication by redistributing mechanical load across the trimer. This specific partitioning—where one part of the assembly (II–III) is stabilized while another (Monomer I) is functionally isolated—offers a mechanistic explanation for the observed attenuation of principal component motions and the overall reduction in dynamic cross-correlations between monomers, which reflect a breakdown in cooperative dynamics essential for propagating conformational signals during oligomerization.

The asymmetric nature of ligand engagement—limited to Monomers II and III—further supports this directional model of filament disruption. This pattern may arise from differential accessibility or conformational adaptability among the interfacial surfaces and could inform future design strategies aimed at selectively targeting filament subunits. Furthermore, while the absence of extensive hydrogen bonding might initially raise concerns regarding interaction specificity, the persistence of hydrophobic contacts and the sustained structural perturbations observed throughout the simulation trajectory underscore the functional relevance of non-polar anchoring in modulating protein-protein assemblies (Fig. 14 & 15).

Taken together, these findings demonstrate that small-molecule binding at the Ib and IIb interfaces can induce targeted structural and dynamic remodeling of the NLRP3PYD filament via asymmetric dynamic partitioning. Among the tested candidates, compound E9 emerges as a particularly promising inhibitor—capable of engaging critical interfacial residues, disrupting oligomeric symmetry, and attenuating the molecular motions that underlie inflammasome assembly. These insights not only validate E9's mechanism of action but also highlight its potential as a lead scaffold for the development of next-generation inflammasome inhibitors.

In conclusion, this study centered on the discovery of novel NLRP3 inhibitors using a multidisciplinary approach. Molecular binding evaluations identified four compounds with notable binding affinities and favorable scoring profiles. These candidates also exhibited promising drug-like properties. Molecular dynamics simulations further revealed valuable insights into the structural stability and dynamic behavior of these four compounds, confirming their robust affinity and enhanced stability relative to reference compounds.

Our results confirmed that compound E9 specifically disrupts PYD–PYD interaction, supporting our initial hypothesis. However, our findings are limited by the in vitro nature of the assays. Additional in vivo validation and cytokine profiling investigating the effect of E9 on IL-18 and caspase-1 activation, cytotoxicity assays and test on animal models (mice, zebrafish, etc.) are required to confirm the therapeutic relevance. Continued investigation is warranted to elucidate the precise mechanisms underlying these molecular interactions and to explore their therapeutic potential more comprehensively.

Methods

Recombinant *E. coli* strain BL21(DE3) was transformed with the pET28a expression vector encoding both native and mutant (S5D) Nluc-PYD and Cluc-PYD, as described previously [32]. The plasmid extraction kit and Ni-NTA agarose column were obtained from Qiagen (Hilden, Germany). Luciferase assay was performed by mixing luciferin (Resem, the Netherlands) and ATP (Sigma).

Cell-Free Assay

The expression and purification of the chimeric proteins

The pET28a constructs encoding Nluc-PYD and Cluc-PYD were transformed *into E. coli* BL21(DE3) cells [32, 34]. A 10 mL starter culture was prepared in LB medium supplemented with

50 μg/mL kanamycin and inoculated with a single transformed colony. The culture was incubated overnight at 37 °C with shaking at 180 rpm. Subsequently, 1 mL of the overnight culture was transferred into 250 mL of 2×YT medium and incubated at 37 °C with shaking until the optical density at 600 nm (OD_{600}) reached approximately 0.6.

To induce protein expression, isopropyl-β-D-1-thiogalactopyranoside (IPTG) was added to a final concentration of 1 mM, and the culture was incubated at 37 °C with shaking for an additional 4 hours. Cells were harvested by centrifugation at 6000 rpm for 20 minutes at 4 °C and resuspended in lysis buffer (20 mM Tris-Base, 500 mM NaCl, 8 M urea, and 5 mM imidazole). Cell disruption was performed on ice using sonication for ten cycles of 10 seconds on and 20 seconds off.

The lysate was centrifuged at 12,000 rpm for 20 minutes to separate soluble proteins from cellular debris. The supernatant was applied to a Ni-NTA agarose column to facilitate binding of His-tagged proteins. After adequate binding time, the column was washed with wash buffer (20 mM Tris-HCl, 500 mM NaCl, 5 mM imidazole) to remove unbound proteins. Target proteins were eluted using elution buffer (20 mM Tris-HCl, 300 mM NaCl, 275 mM imidazole, pH 7.8).

Eluted proteins were analyzed by SDS-PAGE and visualized with Coomassie Brilliant Blue R-250 staining (0.1% w/v in 40% methanol and 10% glacial acetic acid) for 1 hour at room temperature with gentle agitation. Destaining was performed using 40% methanol and 10% acetic acid in distilled water. Gels were scanned and imaged in 8-bit grayscale.

The observed molecular weights corresponded to expected sizes: approximately 33 kDa for Cluc-NLRP3PYD and 60 kDa for Nluc-NLRP3PYD (Fig. 2). The purified proteins were dialyzed against PBS (pH 7.4) and stored at −80 °C for future use.

Screening of Small Molecule Library

To identify inhibitors of the NLRP3 inflammasome complex, a split luciferase assay was employed. NLuc_NLRP3PYD and CLuc_NLRP3PYD constructs were expressed and purified using Ni-NTA agarose affinity chromatography. Screening was performed based onreconstituted luciferase assay to detect compounds that reduced reconstituted luciferase activity, significantly [32, 34, 35, 38].

A library of 1,500 novel organic compounds was tested using a split firefly luciferase assay targeting PYD-PYD homo-interactions. All chemical compounds were originally purified and their chemical structure confirmed by NMR and mass spectrometry in Alexander doomling group. Previously identified inhibitors (QM380 and QM381) served as positive controls to benchmark inhibitory effects. Compounds demonstrating significant inhibition were shortlisted for subsequent in vitro validation [19].

The assay was conducted using black 96-well plates, with protein concentrations optimized for maximal luciferase activity. Each well was loaded with approximately 16 µg of CLuc-NLRP3PYD in 20 mM Tris buffer, followed by an equal volume of library compound dissolved in DMSO, and subsequently 8 µg of NLuc-NLRP3PYD. The first four wells of the first column contained only CLuc-NLRP3PYD, while the last four wells held only NLuc-NLRP3PYD without compound treatment. The first four wells of the previous column served as positive controls, containing both chimeric proteins (CLuc-NLRP3PYD and NLuc-NLRP3PYD) without any compound. The final four wells were used as negative controls, containing both proteins along with an equivalent volume of DMSO to ensure uniform solvent conditions across all wells [29, 43]. Following compound addition, 50 µL of luciferase assay reagent (Promega) was dispensed into each well, and luminescence was measured using the CLARIOstar Plus Multi-Mode Microplate Reader. All compounds were kept frozen at -20℃ at 100 mM stock solution in DMSO. Then, a 5 mM solution

in DMSO prepared for screening. In each well containing 100 µL of final volume , only 5 µL of each individual compound with 5 mM concentration (250 µM final concentration) were added.

An initial screen of 1,500 compounds identified four candidates—B1, G3, E2, and E9—that markedly reduced total luciferase activity. A subsequent confirmation assay was conducted to validate these compounds as potential inhibitors of NLRP3 inflammasome activation.

Structural Analysis

MicroScale Thermophoresis (MST)

Structure refinement, molecular docking, and interaction analysis

Microscale thermophoresis (MST) was utilized to determine the binding affinities of selected inhibitors with high sensitivity and efficiency using the Monolith NT.115 system (NanoTemper Technologies GmbH). MST operates by generating a localized and highly controlled temperature gradient through infrared (IR) laser excitation, enabling thermal conditions that surpass the capabilities of conventional heating methods such as thermal blocks [44]. Binding events are detected by monitoring changes in fluorescence intensity upon IR laser activation, providing a direct measure of molecular interactions [45, 46].

For MST analysis, the purified Cluc-PYD domain of NLRP3 was dialyzed against 0.01 M phosphate-buffered saline (PBS), pH 7.4. Binding affinities of inhibitors E2, E9, B1, and G3 were evaluated using Cluc-PYD protein freshly labeled with His-Tag RED-tris-NTA dye, following the manufacturer's instructions (NanoTemper Technologies GmbH). Fluorescence measurements were performed in MST buffer (50 mM Tris, 250 mM NaCl, pH 7.0) using standard capillaries (K002; NanoTemper Technologies).

The molecular structures of inhibitors B1, G3, E2, and E9 were obtained in mol2 format. In contrast, the crystal structure of the NLRP3PYD peptide (PDB ID: 3QF2) was retrieved from the

Research Collaboratory for Structural Bioinformatics (RCSB) Protein Data Bank (PDB) [34, 47, 48].

Structural preparation included the removal of solvent molecules, addition of polar hydrogen atoms to the protein, merging of non-polar hydrogens with corresponding carbon atoms, identification of rotatable bonds in the ligands, and assignment of Gasteiger partial charges. The processed structures were then converted into pdbqt format using AutoDock Tools (version 1.5.6). Energy minimization of ligands was performed to ensure thermodynamically favorable conformations and optimal spatial arrangements, employing the Lamarckian genetic algorithm implemented in AutoDock [34, 49].

Separate molecular docking analyses were conducted to evaluate selected antagonists known to interact with the target macromolecule. These simulations were individually performed to assess the inhibitory potential of the chosen compounds against the engineered human NLRP3 model, the NLRP3-PYD domain, and Caspase-1 protein. Docking simulations employed a consistent grid box dimension of 46 × 46 × 34 Å, centered at coordinates x = −95.029, y = −128.250, z = −121.544 [50]. The most favorable binding conformations were selected based on binding affinity (ΔG). Subsequent evaluations included calculation of inhibition constants (K) and detailed analysis of molecular interactions within the chosen poses. Protein, ligand, and docking complex visualizations were performed using AutoDock Vina (version 1.1.2) [34, 51].

The output files were initially generated in PDBQT format and subsequently converted to PDB format using UCSF Chimera (version 1.15). For each ligand, the most favorable docking conformation was selected for further analysis. Molecular structures and docking results were visualized using PyMOL (version 2.3.3) and Maestro (version 12.6, Schrödinger, LLC, New York, NY, USA, 2020) [52, 53].

Molecular dynamics simulation

To assess the stability and interaction dynamics of the E9 ligand, molecular dynamics simulations (MDS) were conducted on both the native and ligand-bound states of the NLRP3PYD filament. Chains D, B, and R from the cryo-EM structure (PDB ID: 8ERT[54]) were selected to represent a filament subunit, based on their symmetric interfacial arrangement across six surfaces (Ia–Ib, IIa–IIb, IIIa–IIIb), as shown in Fig. 9. For clarity, these chains were renamed Monomer I, Monomer II, and Monomer III, respectively. The ligand-bound complex was generated by superimposing the docked pose of compound E9 from the prior docking step onto Monomer II, ensuring its placement at the native interface. The resulting structure was subjected to energy minimization to relieve steric clashes and optimize local interactions.

Simulations were performed using the Amber14 force field [55] in the YASARA Suite version 25.9.17 [56], under physiological conditions (pH 7.4, 0.9% NaCl, 298 K). Protonation states of side chains were assigned based on predicted pKa values [57]. The system was solvated in a cubic simulation box with a solvent density of 0.99704 $g \cdot cm^{-3}$, extending 10 Å beyond the protein surface. Long-range electrostatics were treated using the Particle Mesh Ewald (PME) method [58], with an 8 Å cutoff for nonbonded interactions. Simulations were run under NPT ensemble conditions (1 bar, 298 K) [59], with constrained hydrogen atoms and a 4 fs timestep. Snapshots were recorded every 100 ps and analyzed using YASARA macros to extract key structural and dynamic parameters, including Cα-RMSD, RMSF, radius of gyration (Rg), secondary structure evaluation, principal component analysis (PCA) trajectories, and dynamic cross-correlation matrices (DCCM).

ASC Speck Assay

THP1-ASC-GFP cells were seeded at a density of 1×10^6 cells/mL one day before experimentation on 35 mm glass-bottom culture dishes. The following day, the culture medium was replaced with fresh medium containing either an inhibitor (20 μM) or vehicle control (DMSO) and incubated for 30 minutes. Cells were then primed with lipopolysaccharide (LPS, 100 ng/mL) for 3 hours, followed by stimulation with nigericin (5 or 10 μM) for up to 150 minutes. Fluorescence images were acquired using a Cytation 3 imaging system equipped with a 10× objective lens. ASC specks in live cells were quantified from a total of 20 images per condition, obtained from ten random fields in each of two independent experiments.

Author contributions

S. K. performed the experiments, S. H. supervised the experiments, read the final version of manuscript, N.B. analyzed data, M.P. analyzed data, and A.D. provided small molecules library, granted and supervision.

Funding

This research was supported by multiple funding sources awarded to A.D., including the ERA Chair grant ACCELERATOR (No. 101087318), the ERC Advanced Grant AMADEUS (No. 101098001), and the VIDEC grant (No. 872195). Additional support was provided through the National Institute for Cancer Research—Program EXCELES (Project No. LX22NPO5102), funded by Cancer Research Czech Republic, as well as the Dutch Cancer Society (KWF Kankerbestrijding) grant (No. 14712). We thank Prof. Azadeh Ebrahim-Habibi, Dr. Mehri Javid and the Molecular Modeling Group at the Endocrinology and Metabolism Research Institute (EMRI), Tehran University of Medical Sciences, for providing access to computational resources and guidance during MD simulations performed using YASARA. Language editing was supported

by AI-based tools (Copilot and ChatGPT) and subsequently reviewed and approved by the authors, who take full responsibility for the final content.

Competing interests

The authors declare no competing interests.

Data availability statement

The data that support the findings of this study are available on request from the corresponding author.

Ethics declarations

Not applicable.

References

1. Savage, C. D., Lopez-Castejon, G., Denes, A. & Brough, D. NLRP3-inflammasome activating DAMPs stimulate an inflammatory response in glia in the absence of priming which contributes to brain inflammation after injury. *Front. Immunol.* **3**, 288 (2012).

2. Jo, E.-K., Kim, J. K., Shin, D.-M. & Sasakawa, C. Molecular mechanisms regulating NLRP3 inflammasome activation. *Cell Mol. Immunol.* **13**, 148-159 (2016).

3. Mathur, A., Hayward, J. A. & Man, S. M. Molecular mechanisms of inflammasome signaling. *J. Leukoc. Biol.* **103**, 233-257 (2018).

4. Rubartelli, A. DAMP-mediated activation of NLRP3-inflammasome in brain sterile inflammation: the fine line between healing and neurodegeneration. *Front. Immunol.* **5**, 99 (2014).

5. Bulté, D., Rigamonti, C., Romano, A. & Mortellaro, A. Inflammasomes: mechanisms of action and involvement in human diseases. *Cells*. **12**, 1766 (2023).

6. Van Opdenbosch N. & Lamkanfi, M. Caspases in cell death, inflammation, and disease. *Immunity.* **50**, 1352-1364 (2019).

7. Mangan, M. S., Olhava, E. J., Roush, W. R., Seidel, H. M., Glick, G. D. & Latz, E. Targeting the NLRP3 inflammasome in inflammatory diseases. *Nat. Rev. Drug Discov.* **17**, 588-606 (2018).

8. Blevins, H. M., Xu, Y., Biby, S. & Zhang, S. The NLRP3 inflammasome pathway: a review of mechanisms and inhibitors for the treatment of inflammatory diseases. *Front. Aging Neurosci.* **14**, 879021 (2022).

9. Kelley, N., Jeltema, D., Duan, Y. & He, Y. The NLRP3 inflammasome: an overview of mechanisms of activation and regulation. *Int. J. Mol. Sci.* **20**, 3328 (2019).

10. Stutz, A., Horvath, G. L., Monks, B. G. & Latz, E. ASC speck formation as a readout for inflammasome activation. *Methods Mol. Biol.* **1040**, 91-101 (2013).

11. Dick, M. S., Sborgi, L., Rühl, S., Hiller, S. & Broz, P. ASC filament formation serves as a signal amplification mechanism for inflammasomes. *Nat. Commun.* **7**, 1-13 (2016).

12. Takahashi, M. Cell-specific roles of NLRP3 inflammasome in myocardial infarction. *J. Cardiovasc. Pharmacol.* **74**, 188-193 (2019).

13. Stehlik, C., Lee, S. H., Dorfleutner, A., Stassinopoulos, A., Sagara, J. & Reed, J. C. Apoptosis-associated speck-like protein containing a caspase recruitment domain is a regulator of procaspase-1 activation. *J. Immun.* **171**, 6154-6163 (2003).

14. Liepinsh, E., Barbals, R., Dahl, E., Sharipo, A., Staub, E. & Otting, G. The death-domain fold of the ASC PYRIN domain, presenting a basis for PYRIN/PYRIN recognition. *J. Mol. Biol.* **332**, 1155-1163 (2003).

15. Oroz, J., Barrera-Vilarmau, S., Alfonso, C., Rivas, G. & De Alba, E. ASC pyrin domain self-associates and binds NLRP3 protein using equivalent binding interfaces. *J. Biol. Chem.* **291**, 19487-19501 (2016).

16. Liu, X., Pichulik, T., Wolz, O. O., Dang, T. M., Stutz, A., Dillen, C., et al. Human NACHT, LRR, and PYD domain–containing protein 3 (NLRP3) inflammasome activity is regulated by and potentially targetable through Bruton tyrosine kinase. *J. Allergy Clin. Immunol.* **140**, 1054-1067 (2017).

17. Hughes Jr, F. M., Kennis, J. G., Youssef, M. N., Lowe, D. W., Shaner, B. E. & Purves, J. T. The NACHT, LRR and PYD domains-containing protein 3 (NLRP3) inflammasome mediates inflammation and voiding dysfunction in a lipopolysaccharide-induced rat model of cystitis. *J. Clinic. Cell. Immunol.* **7**, 1 (2016).

18. Vande Walle, L., Stowe, I. B., Šácha, P., Lee, B. L., Demon, D., Fossoul, A., et al., MCC950/CRID3 potently targets the NACHT domain of wild-type NLRP3 but not disease-associated mutants for inflammasome inhibition. *PLoS Biol*. **17**, e3000354 (2019).

19. Martín-Sánchez, F., Compan, V. & Pelegrín, P. Measuring NLR oligomerization III: detection of NLRP3 complex by bioluminescence resonance energy transfer. *Methods Mol. Biol.* **1417**, 159-168 (2016).

20. Richards, N., Schaner, P., Diaz, A., Stuckey, J., Shelden, E., Wadhwa, A., et al. Interaction between pyrin and the apoptotic speck protein (ASC) modulates ASC-induced apoptosis. *J. Biol. Chem.* **276**, 39320-39329 (2001).

21. Tangi, T. N., Elmabsout, A. A., Bengtsson, T., Sirsjö, A. & Fransén, K. Role of NLRP3 and CARD8 in the regulation of TNF-α induced IL-1β release in vascular smooth muscle cells. *Int. J. Mol. Med.* **30**, 697-702 (2012).

22. de Alba, E. Structure and interdomain dynamics of apoptosis-associated speck-like protein containing a CARD (ASC). *J. Biol. Chem.* **284**, 32932-32941 (2009).

23. Yang, G., Lee, H. E., Moon, S. J., Ko, K. M., Koh, J. H., Seok, J. K., et al. Direct binding to NLRP3 pyrin domain as a novel strategy to prevent NLRP3-driven inflammation and gouty arthritis. *Arthritis Rheumatol.* **72**, 1192-1202 (2020).

24. Ozaki, E., Campbell, M. & Doyle, S. L. Targeting the NLRP3 inflammasome in chronic inflammatory diseases: current perspectives. *J. Inflamm. Res.* **8**, 15-27 (2015).

25. Jin, C. & Flavell, R. A. Molecular mechanism of NLRP3 inflammasome activation. *J. Clin. Immunol.* **30**, 628-631 (2010).

26. Fu, J. & Wu, H. Structural mechanisms of NLRP3 inflammasome assembly and activation. *Annu. Rev. Immunol.* **41**, (2023).

27. Wu, D., Chen, Y., Sun, Y., Gao, Q., Li, H., Yang, Z., et al., Target of MCC950 in inhibition of NLRP3 inflammasome activation: a literature review. *Inflammation*. **43**, 17-23 (2020).

28. Jiang, H., Gong, T. & Zhou, R. The strategies of targeting the NLRP3 inflammasome to treat inflammatory diseases. *Adv. Immunol.* **145**, 55-93 (2020).

29. Coll, R. C., Robertson, A. A., Chae, J. J., Higgins, S. C., Muñoz-Planillo, R., Inserra, M. C. A small-molecule inhibitor of the NLRP3 inflammasome for the treatment of inflammatory diseases. *Nat. Med.* **21**, 248-255 (2015).

30. Bakhshi, S. & Shamsi, S. MCC950 in the treatment of NLRP3-mediated inflammatory diseases: Latest evidence and therapeutic outcomes. *Int. Immunopharmacol.* **106**, 108595 (2022).

31. McGeough, M. D., Wree, A., Inzaugarat, M. E., Haimovich, A., Johnson, C. D., Peña, C. A., et al. TNF regulates transcription of NLRP3 inflammasome components and inflammatory molecules in cryopyrinopathies. *J. Clin. Invest.* **127**, 4488-4497 (2017).

32. Isazadeh, M., Amandadi, M., Haghdoust, F., Lotfollazadeh, S., Orzáez, M. & Hosseinkhani, S. Split-luciferase complementary assay of NLRP3 PYD-PYD interaction indicates inflammasome formation during inflammation. *Anal. Biochem.* **638**, 114510 (2022).

33. Kim, S. B., Otani, Y., Umezawa, Y. & Tao, H. Bioluminescent indicator for determining protein− protein interactions using intramolecular complementation of split click beetle luciferase. *Anal. Chem.* **79**, 4820-4826 (2007).

34. Moasses Ghafary, S., Soriano-Teruel, P. M., Lotfollahzadeh, S., Sancho, M., Serrano-Candelas, E., Karami, F., et al. Identification of NLRP3PYD homo-oligomerization inhibitors with anti-inflammatory activity. *Int. J. Mol. Sci.* **23**, 1651 (2022).

35. Sebastian-Valverde, M., Wu, H., Al Rahim, M., Sanchez, R., Kumar, K., De Vita, R. J., et al. Discovery and characterization of small-molecule inhibitors of NLRP3 and NLRC4 inflammasomes. *J. Biol. Chem.* **296**, 100597 (2021).

36. Kinra, M., Joseph, A., Nampoothiri, M., Arora, D. & Mudgal, J. Inhibition of NLRP3-inflammasome mediated IL-1β release by phenylpropanoic acid derivatives: in-silico and in-vitro approach. *Eur. J. Pharm. Sci.* **157**, 105637 (2021).

37. Hong, S., Park, S. & Yu, J.-W. Pyrin domain (PYD)-containing inflammasome in innate immunity. *J. Bacteriol. Virol.* **41**, 133-146 (2011).

38. Mostafavi, M., Ataei, F., Hamidieh, A. A. & Hosseinkhani, S. Development of a bioluminescence assay for BIR2-caspase3 interaction through split luciferase complementary assay. *Biochem. Eng. J.* **186**, 108584 (2022).

39. Hattori, M. & Ozawa, T. Split luciferase complementation for analysis of intracellular signaling. *Anal. Sci.* **30**, 539-544 (2014).

1. 40. Hosseinkhani, S., Amandadi, M., Ghanavatian, P., Zarein, F., Ataei, F., Nikkhah, M. & Vandenabeele, P. Harnessing luciferase chemistry in regulated cell death modalities and autophagy: overview and perspectives. *Chem Soc Rev* **53**, 11557–11589 (2024).

41. Villalobos, V., Naik, S. & Piwnica-Worms, D. Detection of protein-protein interactions in live cells and animals with split firefly luciferase protein fragment complementation. *Methods Mol. Biol.* **439**, 339-352 (2008).

42. Paulmurugan, R. & Gambhir, S. S. Firefly luciferase enzyme fragment complementation for imaging in cells and living animals. *Anal. Chem.* **77**, 1295-1302 (2005).

43. Xiang, Y., Zhao, M. M., Sun, S., Guo, X. L., Wang, Q., Li, S. A., et al. A high concentration of DMSO activates caspase-1 by increasing the cell membrane permeability of potassium. *Cytotechnology* **70**, 313-320 (2018).

44. Lee, K. K., Ohyama, T., Yajima, N., Tsubuki, S. & Yonehara, S. MST, a physiological caspase substrate, highly sensitizes apoptosis both upstream and downstream of caspase activation. *J. Biol. Chem.* **276**, 19276-19285 (2001).

45. Wienken, C. J., Baaske, P., Rothbauer, U., Braun, D. & Duhr, S. Protein-binding assays in biological liquids using microscale thermophoresis. *Nat. Commun.* **1**, 100 (2010).

46. Jerabek-Willemsen, M., André, T., Wanner, R., Roth, H. M., Duhr, S., Baaske, Ph., et al. MicroScale Thermophoresis: Interaction analysis and beyond. *J. Mol. Struct.* **1077**, 101-113 (2014).

47. Berman, H. M., Battistuz, T., Bhat, T. N., Bluhm, W. F., Bourne, P. E., Burkhardt, K., et al. The protein data bank. *Acta Crystallogr D Biol. Crystallogr.* **58**, 899-907 (2002).

48. Berman, H. M., Battistuz, T., Bhat, T. N., Bluhm, W. F., Bourne, P. E., Burkhardt, K., et al. The protein data bank. *Acta Crystallogr D Biol Crystallogr.* **58**, 899-907 (2002).

49. Sanner, M. F. Python: a programming language for software integration and development. *J. Mol. Graph Model.* **17**, 57-61 (1999).

50. Trott, O. & Olson, A. J. AutoDock Vina: improving the speed and accuracy of docking with a new scoring function, efficient optimization, and multithreading. *J. Comput. Chem.* **31**, 455-461 (2010).

51. Patil, S. M., Manu, G., Shivachandra, J. C., Anil Kumar, K. M., Vigneswaran, J., Ramu, R., et al. Computational screening of benzophenone integrated derivatives (BIDs) targeting the NACHT

domain of the potential target NLRP3 inflammasome. *Adv. Cancer Biol. - Metastasis.* **5**, 100056 (2022).

52. Burley, S. K., Berman, H. M., Kleywegt, G. J., Markley, J. L., Nakamura, H. & Velankar, S. Protein Data Bank (PDB): the single global macromolecular structure archive. *Methods Mol. Biol.* **1607**, 627-641 (2017).

53. Shaker, B., Yu, M. S., Lee, J., Lee, Y., Jung, C. & Na, D. User guide for the discovery of potential drugs via protein structure prediction and ligand docking simulation. *J. Microbiol.* **58**, 235-244 (2020).

54. Xiao L, Magupalli VG, Wu H. Cryo-EM structures of the active NLRP3 inflammasome disc. Nature. 2023;613(7944):595–600.

55. Hornak V, Abel R, Okur A, Strockbine B, Roitberg A, Simmerling C. Comparison of multiple Amber force fields and development of improved protein backbone parameters. Proteins. 2006;65(3):712–25.

56. Krieger E, Vriend GJB. YASARA View—molecular graphics for all devices—from smartphones to workstations. 2014;30(20):2981–2.

57. Krieger E, Nielsen JE, Spronk CA, Vriend G. Fast empirical pKa prediction by Ewald summation. J Mol Graph Model. 2006;25(4):481–6.

58. Essmann U, Perera L, Berkowitz ML, Darden T, Lee H, Pedersen LGJTJocp. A smooth particle mesh Ewald method. 1995;103(19):8577–93.

59. Krieger E, Vriend G. New ways to boost molecular dynamics simulations. J Comput Chem. 2015;36(13):996–1007.

Legends to figures

Fig 1. Structural representation of the NLRP3 PYD monomer, interaction surfaces, and modeled filament assembly (based on PDB ID: 8ERT). (A) Three-dimensional structure of a single NLRP3 PYD subunit shown in cartoon form, with helices depicted in navy blue and connecting loops in cyan. (B) Interaction surfaces that mediate PYD–PYD contacts within the filament. Each surface is highlighted in a distinct color—Ia (red) pairing with Ib (green), IIa (magenta) pairing with IIb (cyan), and IIIa (yellow) pairing with IIIb (blue)—illustrating the complementary interfaces that engage during filament formation. (C) Modeled NLRP3 PYD filament visualized in cartoon representation, showing the helical arrangement and the repeating pattern of interacting PYD subunits that give rise to the polymeric filament structure.

Fig. 2. SDS-PAGE shows the purified NLUC-NLRP3PYD and CLUC-NLRP3PYD proteins and their mutant counterparts (S5D). "L" indicates lysate of cell extract, "P" indicate its purified counterpart and "M" is molecular weight marker.

Fig. 3. The time dependent effect of the selected compounds on luciferase activity. In each well, immediately after incubation of proteins with selected compounds substrates were added and luciferase activity was monitored without extra addition of substrates. Luciferase activity was monitored at defined time intervals (0, 3, 6, 9, and 12 minutes) following compound administration. All compounds were tested at constant concentrations throughout the experiment. Among the tested compounds, B1, G3, E2, and E9 exhibited a reduction in luciferase signal over time, consistent with disruption of PYD–PYD interaction.

Fig. 4. Dose-response curves for compounds B1, G3, E2, and E9 were constructed based on initial activity measurements at escalating ligand concentrations.

Fig. 5. Molecular docking of hit compounds to the NLRP3 PYD. (A) Chemical structures of B1, E2, E9, and G3 with their molecular formulas and molecular weights. (B) Three-dimensional docking poses of each ligand in the interaction region, represented using YASARA. PYD interfaces are colored as follows: Ia (red), Ib (green), IIa (magenta), IIIa (yellow), IIb (cyan), and IIIb (blue). Ligands are shown as colored ball-and-stick models. (C) Two-dimensional interaction maps generated using LigPlot, where hydrogen bonds are depicted as green dashed lines and hydrophobic interactions as red spoked arcs surrounding the participating residues.

Fig. 6. Dose-response curve, raw capillary data, and MST trace analysis of NlucPYD_NLRP3 (S5D mutant) in complex with its Cluc-labeled counterpart, which is deficient in homotypic interaction capability. All capillary fluorescence signals remained within ±20% variation.

Fig. 7. Comparative analysis of Dose-Response Curves for E2, E9, G3, and B1 Ligands at 25 °C and 45 °C To ensure consistency across all experimental conditions, the concentrations of the pyrin domain (PYD) protein and the ligands were uniformly standardized at 50 nM and 200 μM, respectively. Comparative analysis of the dose-response curves revealed that the dissociation constant (Kd) for the PYD–E9 complex was markedly lower than that observed for the other ligand-protein combinations. This suggests that E9 exhibits a stronger binding affinity and more potent inhibitory activity, as evidenced by a pronounced reduction in luminescence in the presence of the E9 ligand.

Fig. 8. E9 inhibits ASC speck formation. (A) Representative live-cell images of THP-1-ASC-GFP cells acquired 120 minutes after stimulation with nigericin (5 μM) under the indicated treatment conditions. Fluorescence images (left) show ASC speck formation; corresponding bright-field images (middle) and merged overlays (right) are also presented. (B) Quantification of ASC speck

formation in THP-1-ASC-GFP cells treated with E9 (20 μM) and co-stimulated with LPS (100 ng/mL) and nigericin (10 μM). Data are expressed as mean ± SD. Statistical significance was determined using student t-test vs. LPS/nigericin-treated control).

Fig. 9. Native and Ligand-bound NLRP3PYD Filament Subunits. Ribbon representations of the filament subunit in native (right) and ligand-bound (left) states prior to molecular dynamics simulation. Each subunit comprises three monomers (Monomer I, II, III), extracted from chains D, B, and R of the cryo-EM structure (PDB ID: 8ERT). The E9 ligand is shown bound at the interface between monomers, illustrating its interfacial positioning and potential inhibitory function.

Fig 10. Molecular dynamics (MD) simulation analyses of native (maroon) and E9 ligand-bound (cyan) NLRP3-PYD filaments. (A) Backbone Cα-RMSD over 100 ns. The ligand-bound filament displays larger RMSD fluctuations than the native filament, indicating decreased structural stability and increased overall flexibility upon ligand binding. (B) Radius of gyration (Rg). Both systems show comparable fluctuation patterns; however, the ligand-bound state maintains a slightly higher Rg, suggesting a less compact conformation and enhanced structural flexibility. (C) Per-residue RMSF for monomers I–III. Increased fluctuations are observed across all monomers in the ligand-bound state. (D) Structural superposition after MD simulation. The overlay of native and ligand-bound filaments highlights ligand-induced conformational deviations throughout the filament. These conformational shifts are especially evident in monomer II, which undergoes more noticeable structural displacement compared to monomers I and III, consistent with its higher RMSF values. The ligand remains retained within the binding interface, confirming that increased RMSD arises from filament-wide flexibility rather than ligand dissociation.

Fig. 11. Disruption of NLRP3 Inflammasome Assembly via Ligand-Induced Remodeling of Pyrin Domain Interfaces. (A) Ligand RMSD analysis showing ligand movement and internal conformational changes over the MD trajectory. Despite notable early displacement, the ligand remains stably positioned throughout approximately the last third of the simulation, indicating adoption of a sustained and energetically favorable binding pose. (B) Structural superposition of the filament subunit before (green) and after (magenta) MD simulation, highlighting a pronounced displacement—particularly in Monomer II—as the subunit accommodates ligand engagement. (C) Close-up view of the ligand-binding interface illustrating spatial rearrangement of key contact regions following simulation. (D) LigPlot 2D interaction maps before (left) and after (right) MD simulation, showing the shift in contact patterns and the emergence of a remodeled interaction environment while the ligand remains associated with the binding site.

Fig. 12. Principal Component Analysis of Trimer Dynamics. (A) Temporal Distributions of Principal Components (PC1–PC3): The Native filament (left) explores a substantially wider amplitude range, whereas the Ligand-Bound filament (right) exhibits a compressed amplitude scale. Ligand binding markedly attenuates PC1 fluctuations (blue trace) and redistributes the variance across PC2 and PC3 (yellow and green traces), altering their temporal patterns. These changes indicate that ligand engagement dampens the dominant collective motion while reshaping the contributions of secondary modes to the trimer's conformational sampling. (B) Conformational Space Projections (Scatter Plots): Projection of the simulation trajectories onto PC pairs (PC1 vs. PC2 and PC1 vs. PC3) reveals that the Native state (top) spans a broad conformational space, whereas the Ligand-Bound state (bottom) exhibits tighter clustering. This reflects reduced conformational diversity and enhanced structural constraint upon ligand binding.

Fig. 13. Ligand-induced reprogramming of intra- and inter-monomer dynamics in the trimer. (A) DCCM matrices for the Native and Ligand-Bound states illustrate asymmetric redistribution of dynamic couplings across Monomers I, II, and III. Each 3×3 grid visualizes intra- and inter-monomer correlations, with values ranging from –1 (perfectly anti-correlated) to +1 (perfectly correlated); yellow indicates positive correlation and blue indicates anti-correlation. The matrices include clear annotations demarcating intra-monomer regions (diagonal blocks) and inter-monomer regions (off-diagonal blocks). In the Ligand-Bound state, the II/II and III/III blocks show qualitative shifts in internal correlation patterns, while the II–III interface exhibits expanded bright-yellow regions reflecting strengthened positive coupling. Monomer I displays enhanced internal coherence within the I/I block together with extensive blue anti-correlations across its interfaces with Monomers II and III, consistent with anti-phase motion and stress-driven dynamic decoupling. (B) Structural correlation networks visualizing the redistribution of dynamical couplings. Red connecting lines represent strongly correlated residue pairs. The dense accumulation of these lines within Monomer I indicates dynamic isolation and effective decoupling from the filament core. Conversely, the reduction of internal networks in Monomer III and their redistribution towards Monomer II reflects strengthened inter-monomer coupling. The ligand (green mesh) functions as a dynamic bridge, locally stabilizing the II–III core.

Fig. 14. Secondary structure dynamics of Monomer II during simulation. In the native state (top), helices remain stable, while in the ligand-bound state (bottom), increased fluctuations and transitions between helix, coil, turn, and sheet are observed, particularly in residues 30–55. These changes suggest ligand binding induces local destabilization and increased structural plasticity in

Monomer II, potentially impacting filament flexibility and function. Plots were generated using YASARA software.

Fig. 15. The effect of E9 ligand on the stability and conformation of the NLRP3PYD filament subunit. (A) RMSD profiles showing ligand movement and conformational change during molecular dynamics simulation, after superposition on the receptor and ligand, respectively. (B) Structural superposition of the ligand-bound filament subunit (post-simulation, purple) onto the native form (gray), showing a significant displacement of Monomer II upon ligand binding. (C) Close-up view of the ligand-binding interface, highlighting spatial rearrangement and key contact regions. (D) 2D interaction map (LigPlot) of the E9 ligand with surrounding residues, highlighting hydrophobic interactions with key interface residues.

Figures

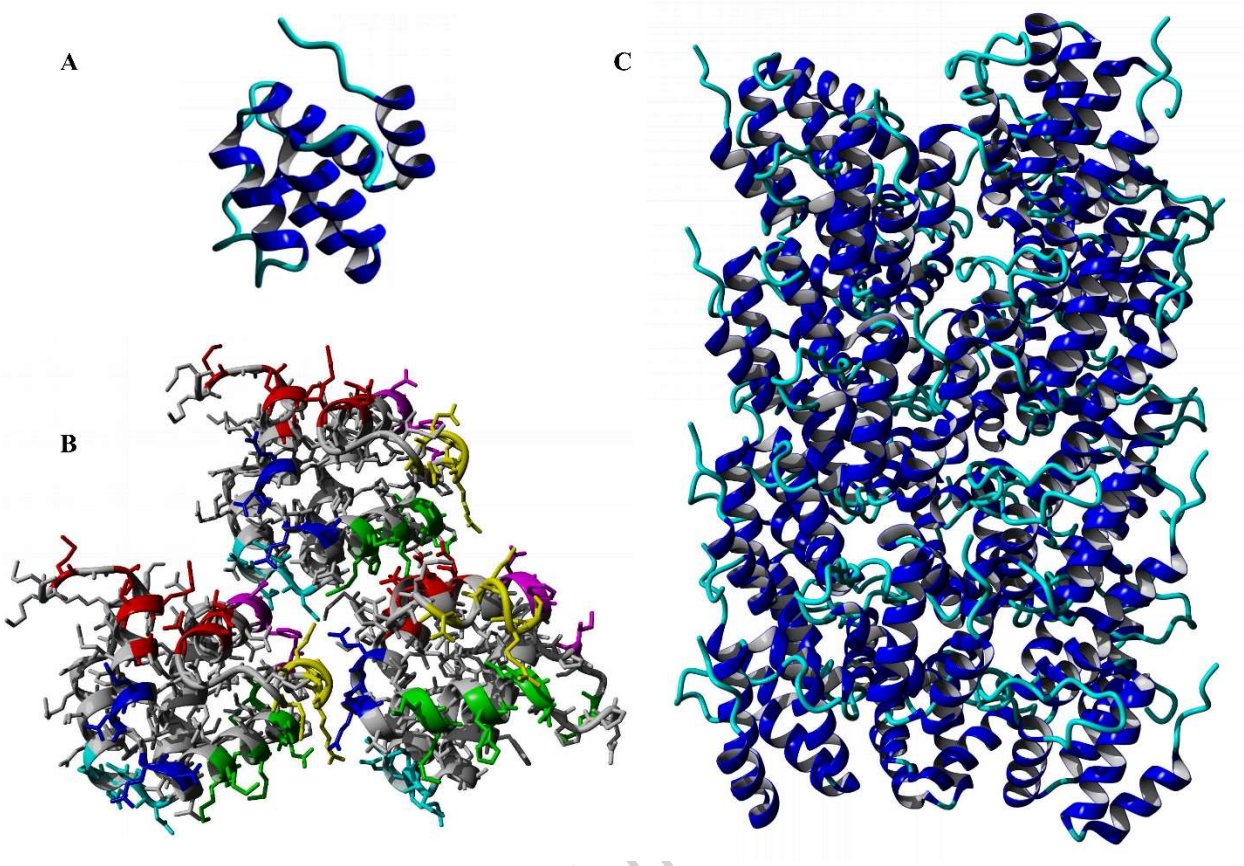

Fig. 1

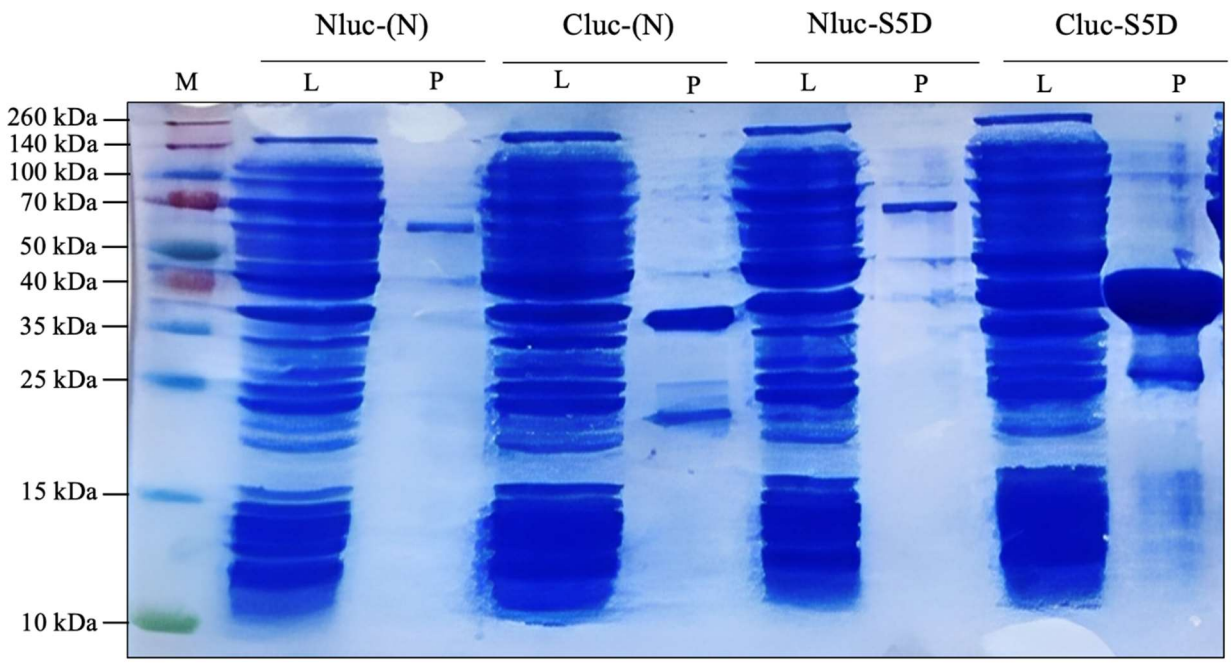
Nluc-(N)
Cluc-(N)
Nluc-S5D
Cluc-S5D
M
L
P
L
P
L
P
L
P
260 kDa
140 kDa
100 kDa
70 kDa
50 kDa
40 kDa
35 kDa
25 kDa
15 kDa
10 kDa

Fig. 2

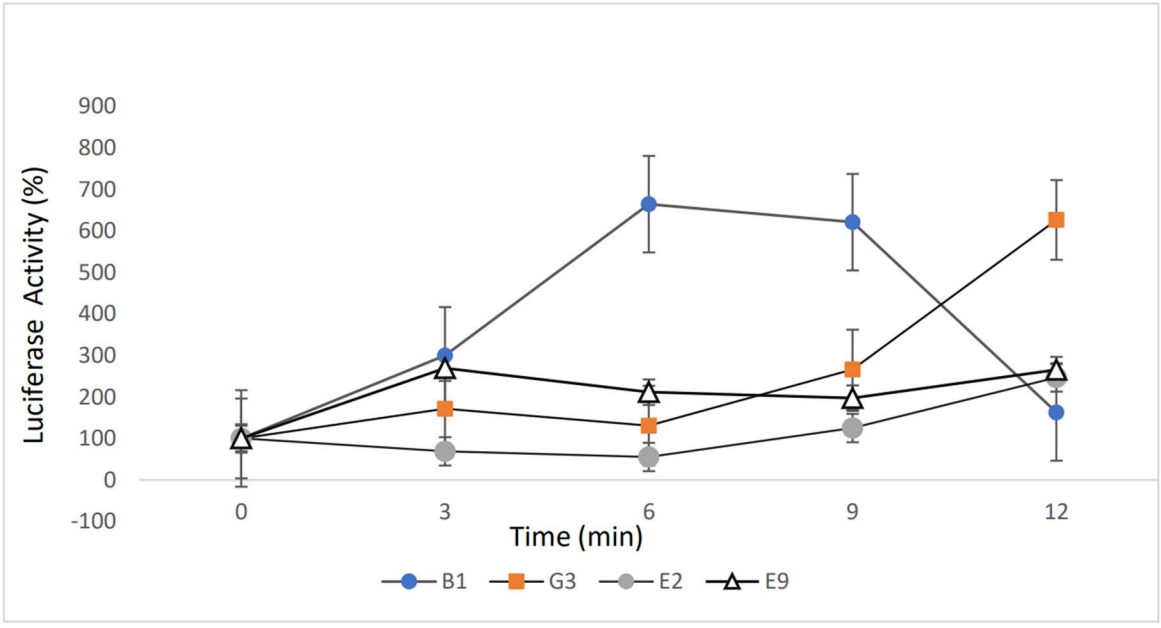
Luciferase Activity (%)
900
800
700
600
500
400
300
200
100
0
-100
0
3
6
9
12
Time (min)
B1
G3
E2
E9

Fig. 3

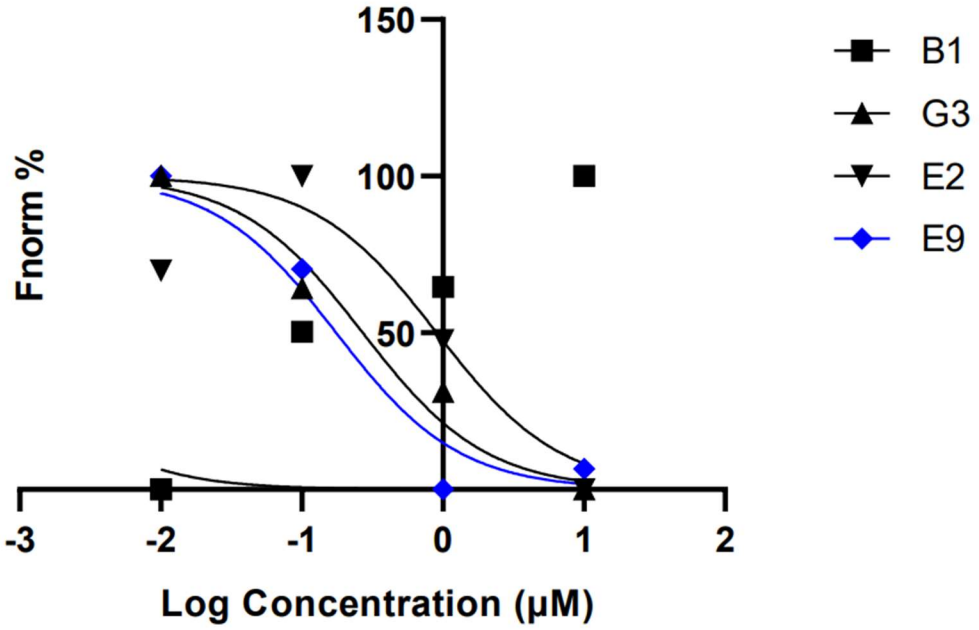

Fig. 4

A

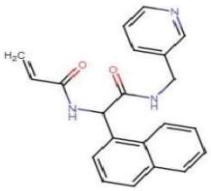

B1 – 994: C21H19N3O2
345.4 g/mol

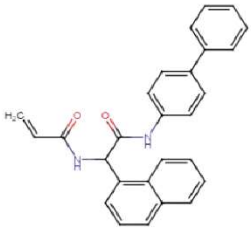

E2 -1031: C27H22N2O2
406.49 g/mol

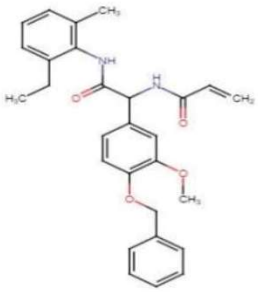

E9 - 1038: C28H30N2O4
458.56 g/mol

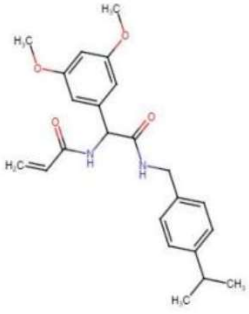

G3 - 1056: C23H28N2O4
396.49 g/mol

B

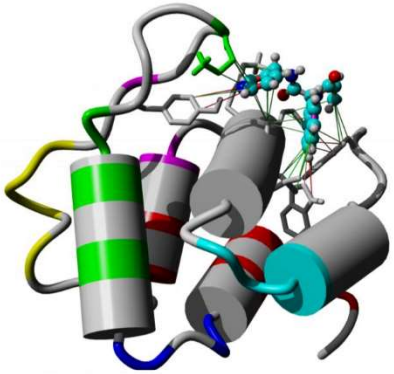

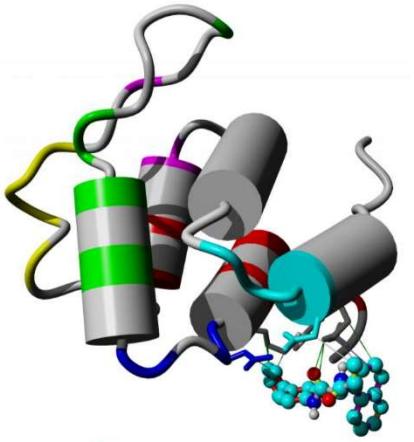

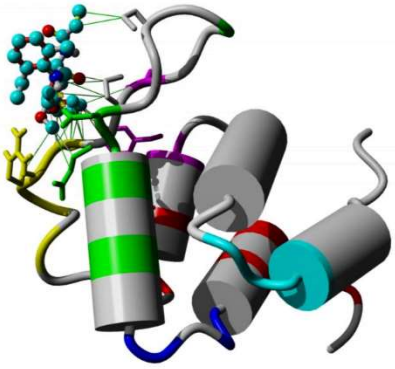

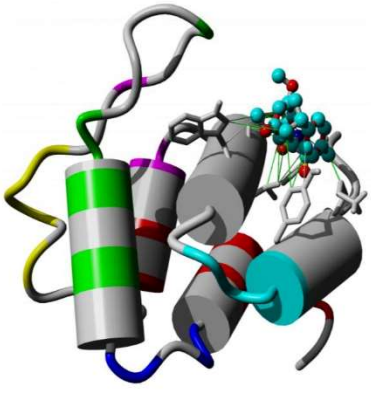

C

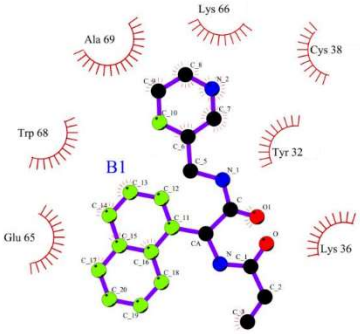

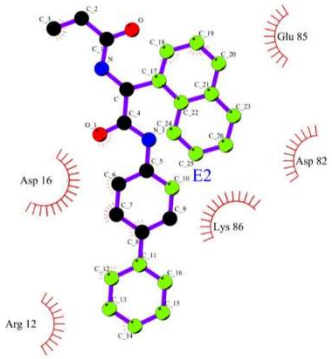

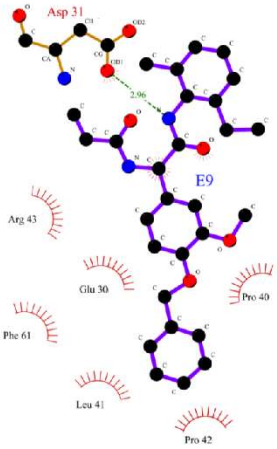

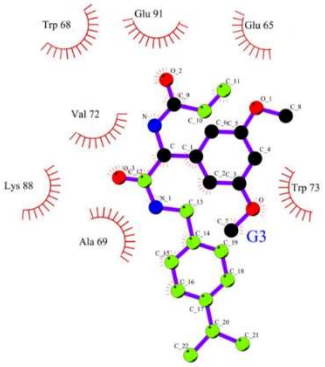

Fig. 5

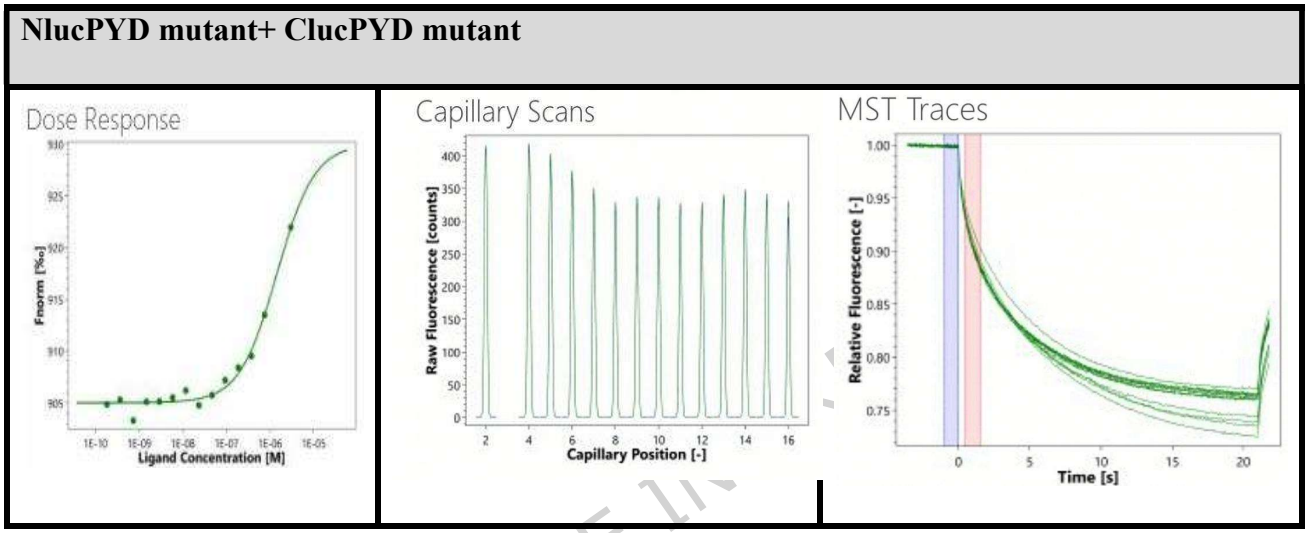

Fig. 6

Ligand type	25 °C	45 °C
PYD – E2	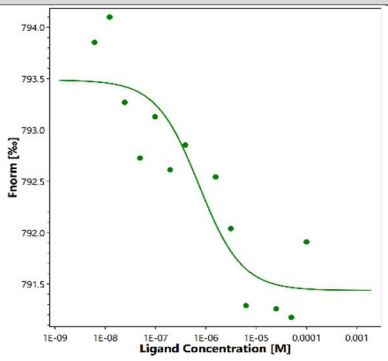	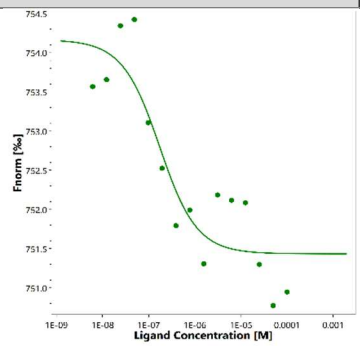
PYD – E9	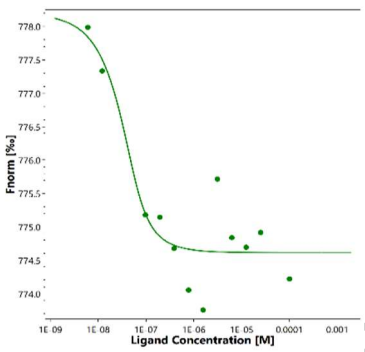	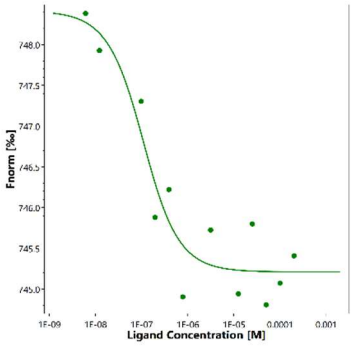
PYD- B1	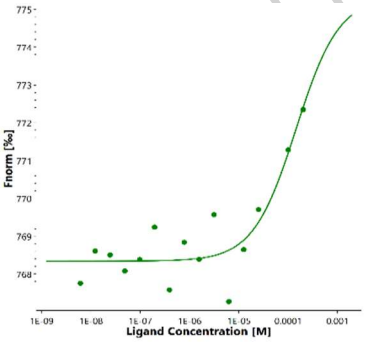	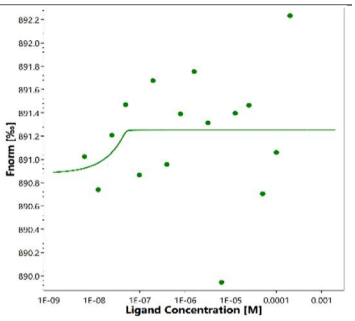
PYD- G3	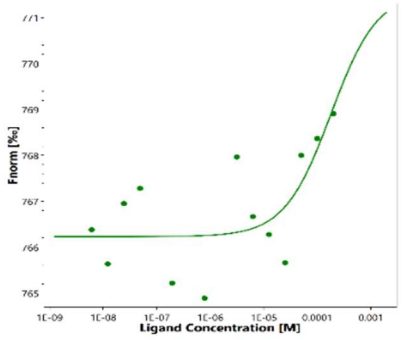	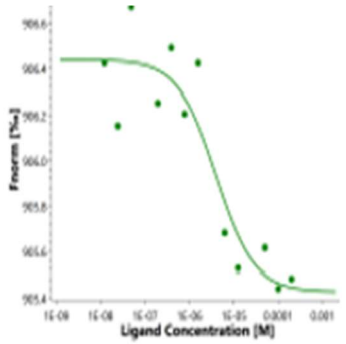

Fig. 7

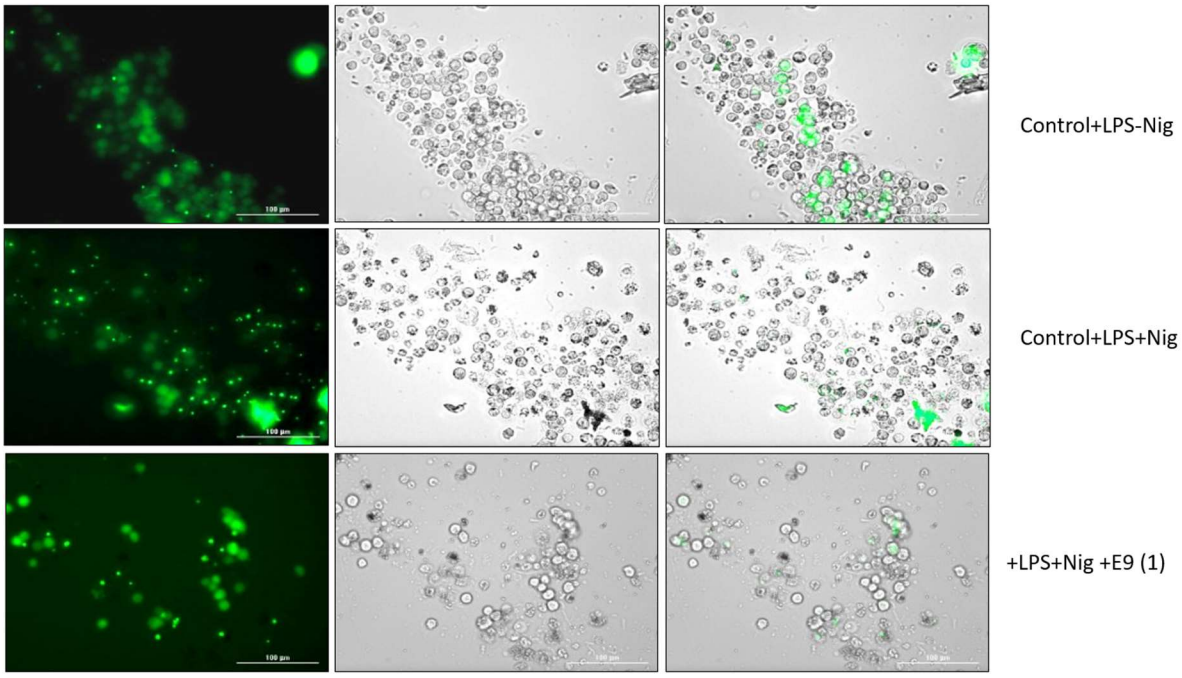
Control+LPS-Nig
Control+LPS+Nig
+LPS+Nig +E9 (1)

Fig. 8A

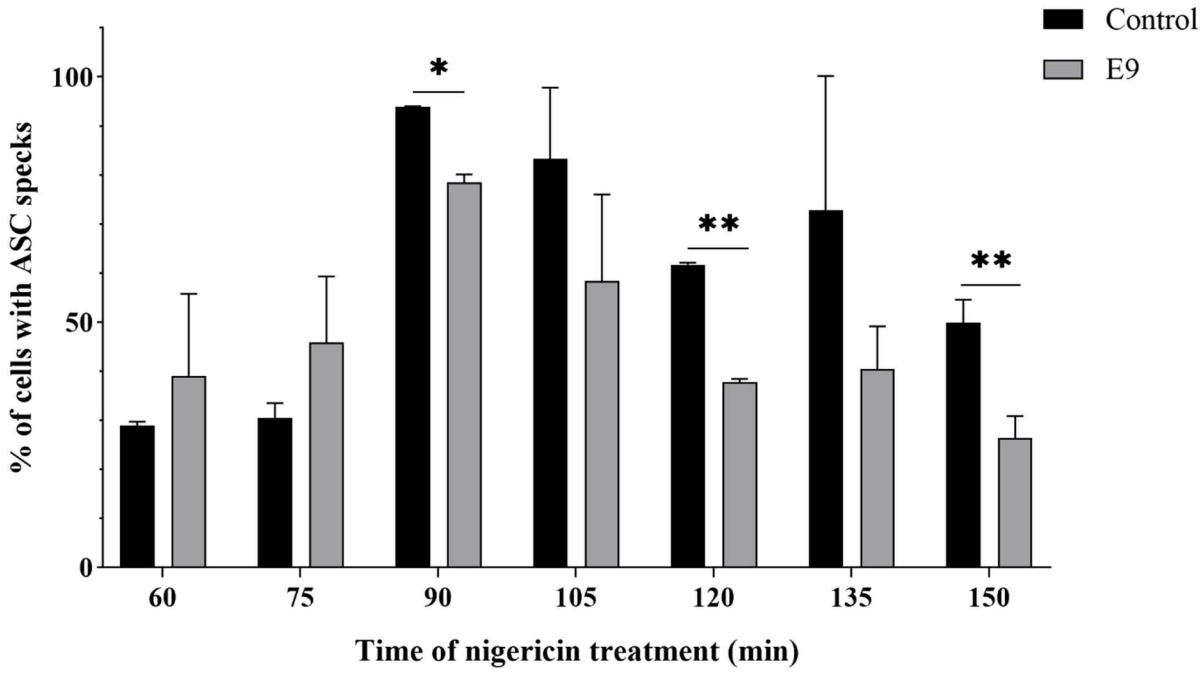
Control
E9
% of cells with ASC specks
100
50
0
*
**
**
60
75
90
105
120
135
150
Time of nigericin treatment (min)

Fig. 8B

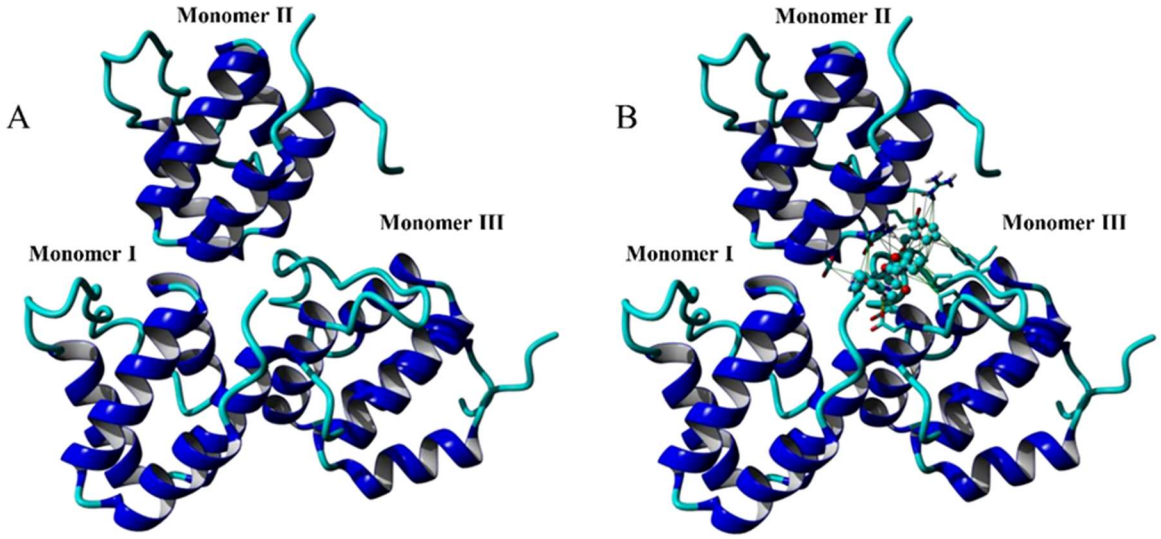

Fig. 9

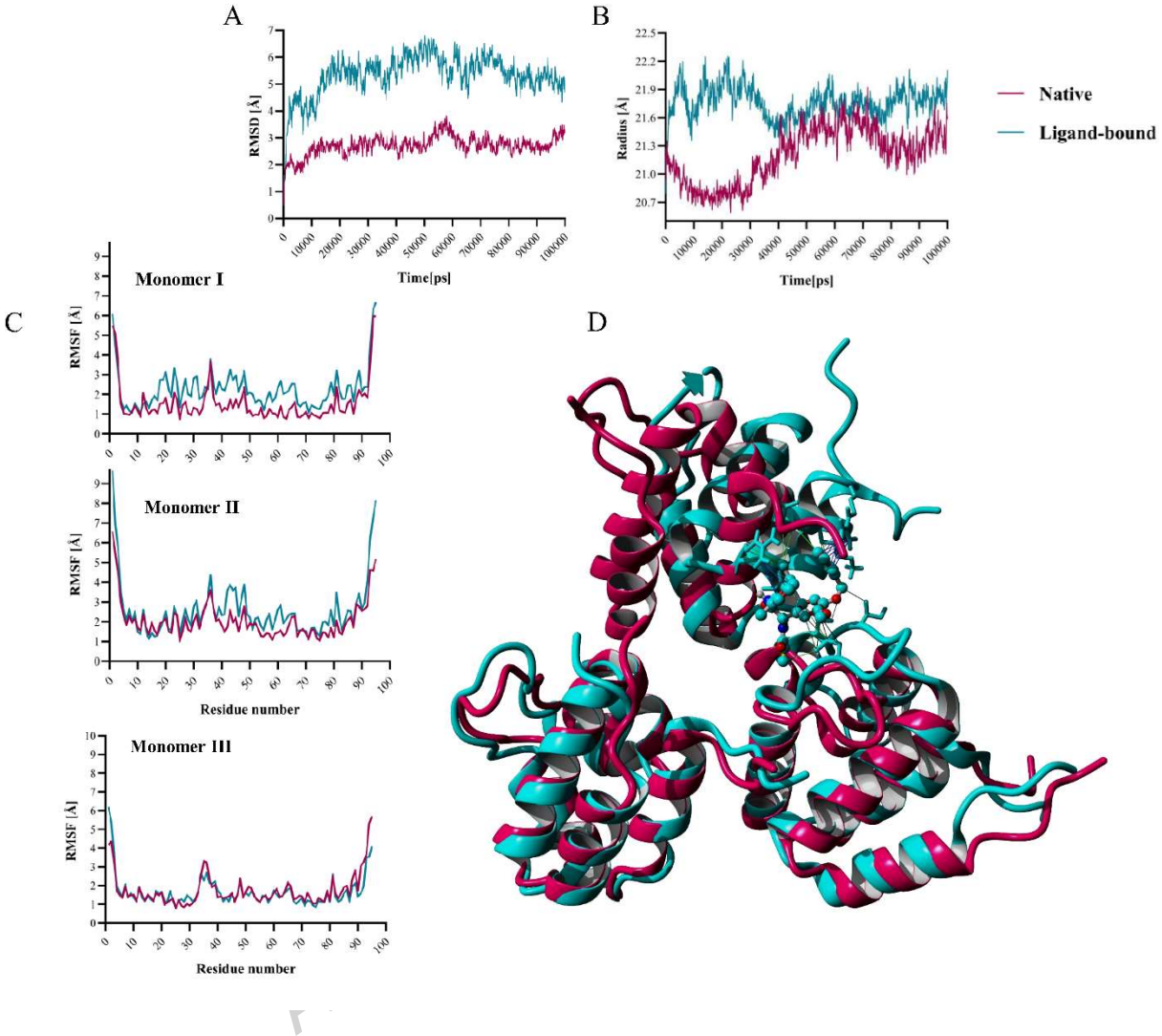
A
RMSD [Å]
Time[ps]
B
Radius [Å]
Time[ps]
Native
Ligand-bound
C
Monomer I
RMSF [Å]
Monomer II
RMSF [Å]
Residue number
Monomer III
RMSF [Å]
Residue number
D

Fig. 10

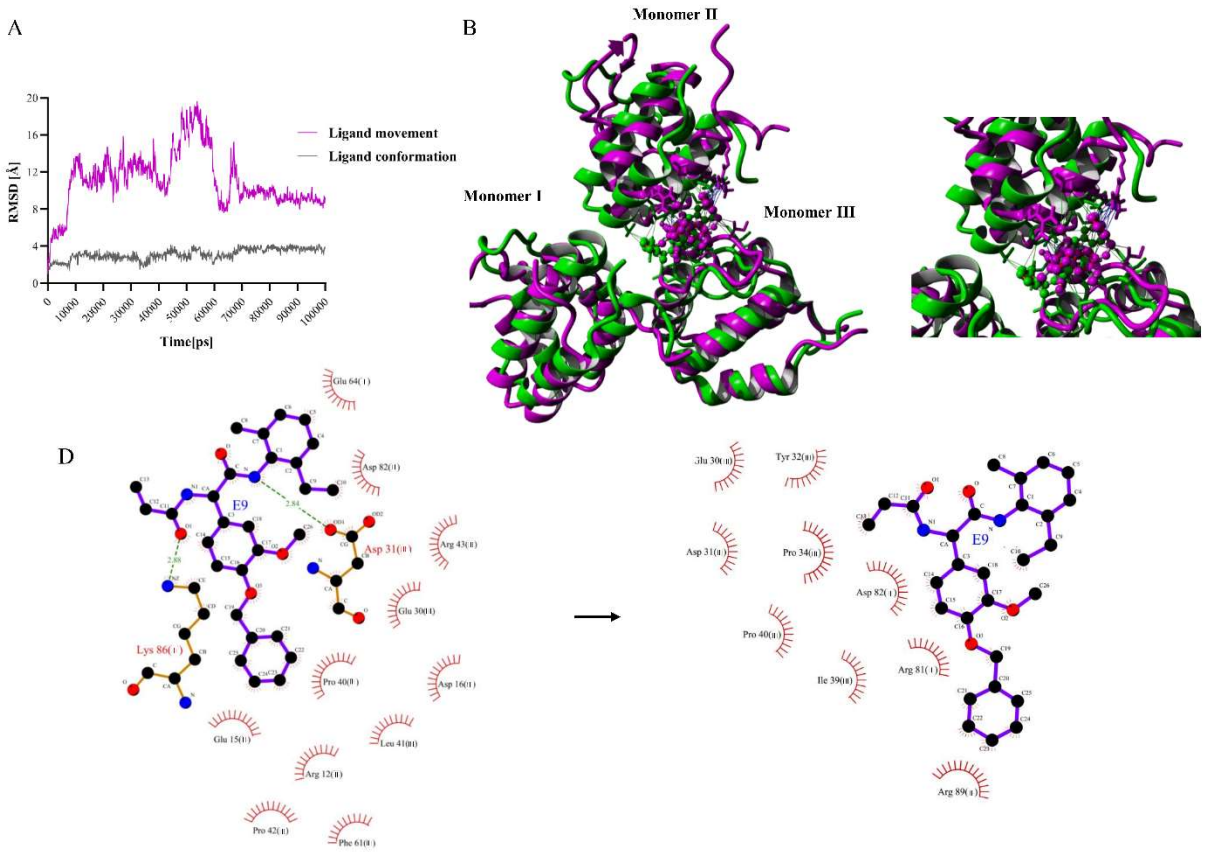

Fig. 11

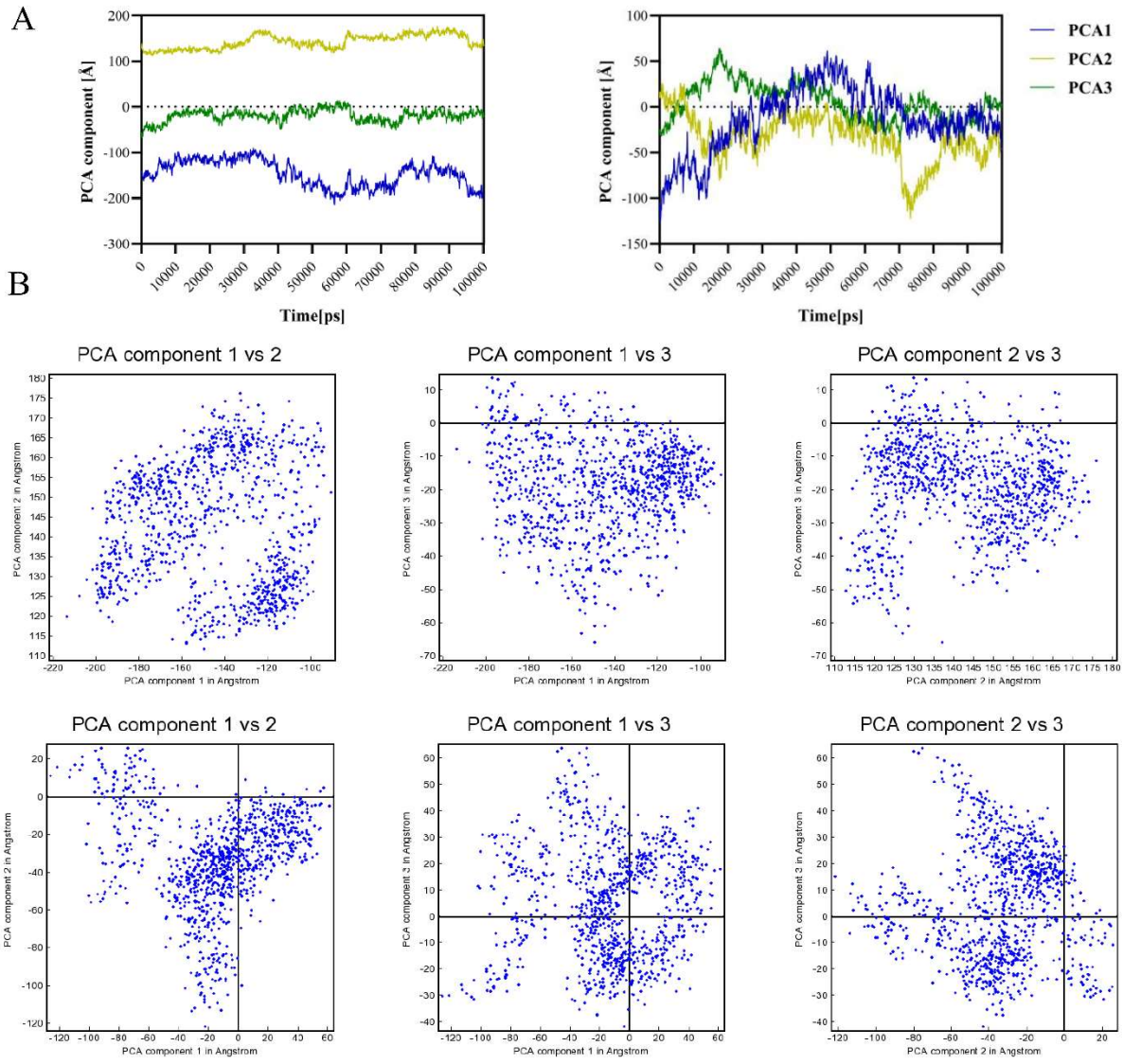
A
PCA component [Å]
Time[ps]
PCA1
PCA2
PCA3
B
PCA component 1 vs 2
PCA component 1 vs 3
PCA component 2 vs 3
PCA component 2 in Angstrom
PCA component 3 in Angstrom
PCA component 1 in Angstrom
PCA component 1 vs 2
PCA component 1 vs 3
PCA component 2 vs 3
PCA component 2 in Angstrom
PCA component 3 in Angstrom
PCA component 1 in Angstrom

Fig. 12

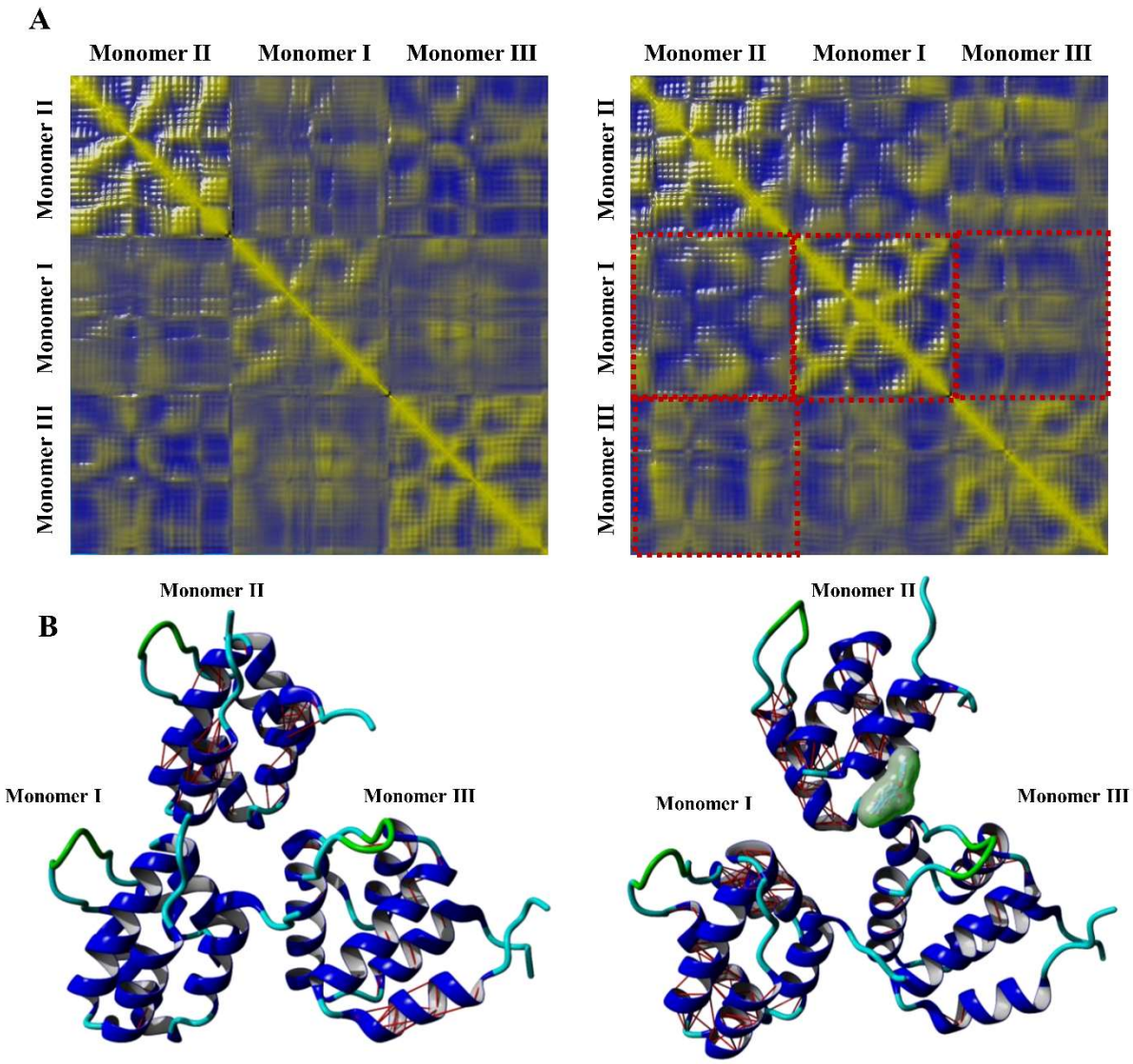
A
Monomer II
Monomer I
Monomer III
Monomer II
Monomer I
Monomer III
Monomer II
Monomer I
Monomer III
B
Monomer II
Monomer I
Monomer III
Monomer II
Monomer I
Monomer III

Fig. 13

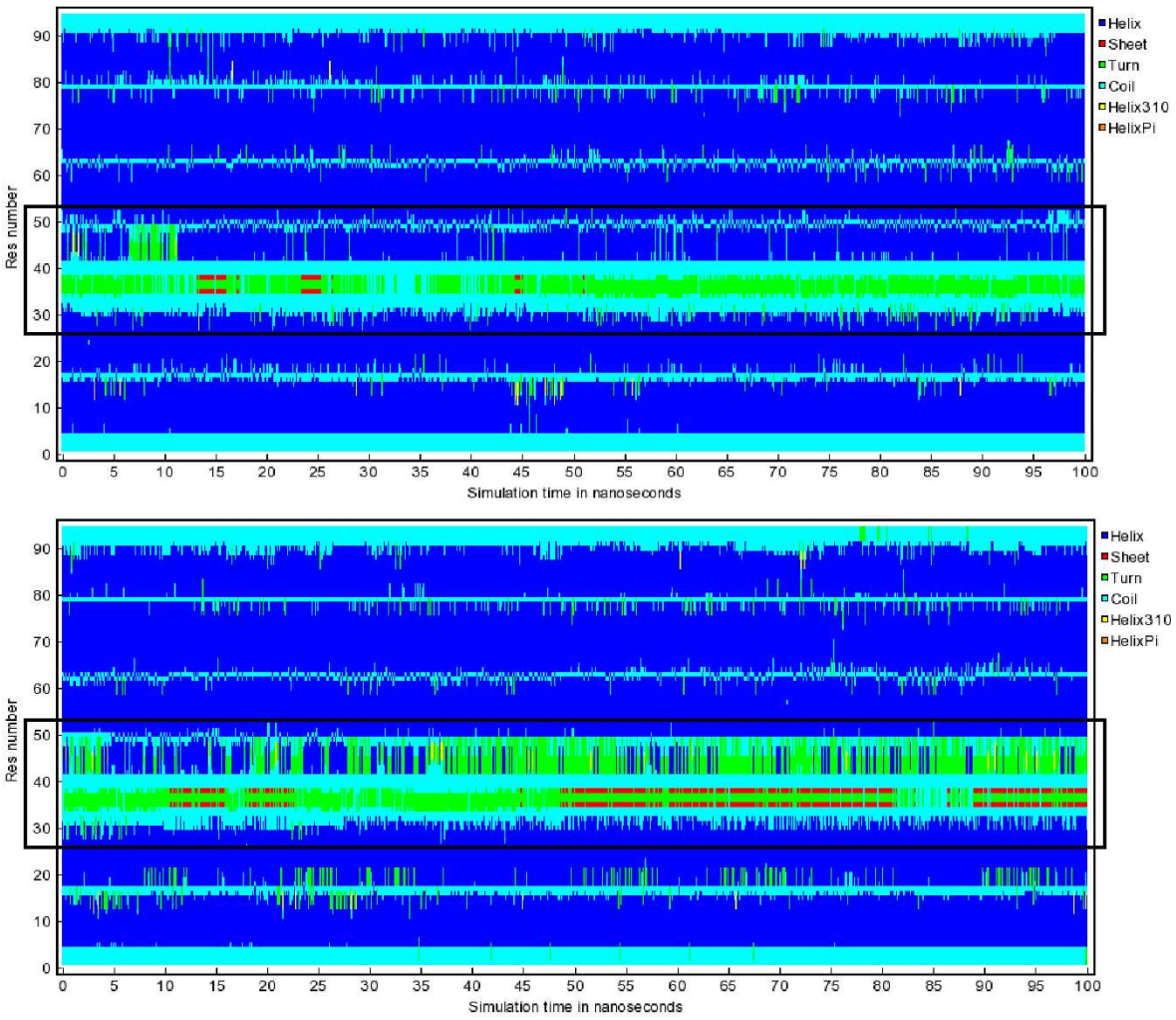
Helix
Sheet
Turn
Coil
Helix310
HelixPi
Res number
Simulation time in nanoseconds
Helix
Sheet
Turn
Coil
Helix310
HelixPi
Res number
Simulation time in nanoseconds

Fig. 14

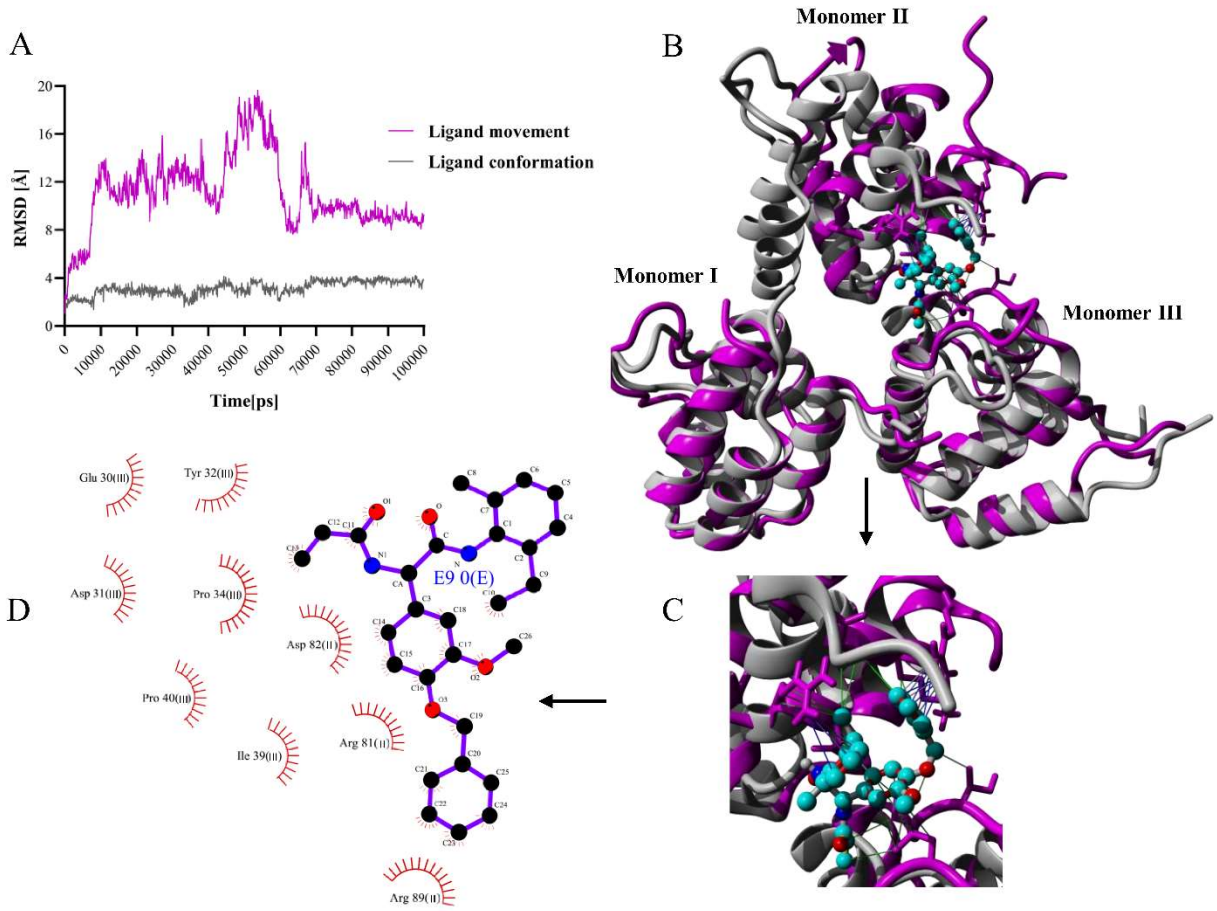
A
RMSD [Å]
Time[ps]
Ligand movement
Ligand conformation
B
Monomer II
Monomer I
Monomer III
C
D
E9 0(E)
Glu 30(III)
Tyr 32(III)
Asp 31(III)
Pro 34(III)
Asp 82(II)
Pro 40(III)
Ile 39(III)
Arg 81(II)
Arg 89(II)

Fig. 15